Princeton Plasma Physics Laboratory

PPPL- 4500

PPPL- 4500

Measurements of Beam Ion Loss from the Compact Helical System

D. S. Darrow, M. Isobe, Takashi Kondo, M. Sasao, and the CHS Group
National Institute for Fusion Science, Toki, Gifu, Japan

March, 2010

PPPL
PRINCETON PLASMA
PHYSICS LABORATORY

Prepared for the U.S. Department of Energy under Contract DE-AC02-09CH11466.

Princeton Plasma Physics Laboratory
Report Disclaimers

Full Legal Disclaimer

Trademark Disclaimer

PPPL Report Availability

Princeton Plasma Physics Laboratory:

http://www.pppl.gov/techreports.cfm

Office of Scientific and Technical Information (OSTI):

http://www.osti.gov/bridge

Related Links:

U.S. Department of Energy

Office of Scientific and Technical Information

Fusion Links

Measurements of Beam Ion Loss from the Compact Helical System

D. S. Darrow[1], M. Isobe, Takashi Kondo[2], M. Sasao[3], and the CHS group
National Institute for Fusion Science, Toki, Gifu, Japan

[1]Also Princeton Plasma Physics Laboratory, Princeton, New Jersey, USA (Present affiliation: Princeton Plasma Physics Laboratory, Princeton, New Jersey, USA)
[2]Graduate University for Advanced Studies, Toki, Gifu, Japan (Present affiliation: Shimadzu Corp.)
[3]Present affiliation: Department of Quantum Engineering, Tohoku University, Sendai, Japan

Abstract

Beam ion loss from the Compact Helical System (CHS) has been measured with a scintillator-type probe. The total loss to the probe, and the pitch angle and gyroradius distributions of that loss, have been measured as various plasma parameters were scanned. Three classes of beam ion loss were observed at the probe position: passing ions with pitch angles within 10° of those of transition orbits, ions on transition orbits, and ions on trapped orbits, typically 15° or more from transition orbits. Some orbit calculations in this geometry have been performed in order to understand the characteristics of the loss. Simulation of the detector signal based upon the following of orbits from realistic beam deposition profiles is not able to reproduce the pitch angle distribution of the losses measured. Consequently it is inferred that internal plasma processes, whether magnetohydrodynamic modes, radial electric fields, or plasma turbulence, move previously confined beam ions to transition orbits, resulting in their loss.

I. Introduction and Motivations

Helical plasma magnetic confinement systems have been the subject of continued study since the first days of the controlled thermonuclear fusion program.[1] Although plasmas in such systems have not approached the conditions necessary for a fusion reactor as closely as have tokamak plasmas, the fact that such plasmas do not require any internal plasma current and are not subject to disruptions has made them the subject of renewed interest in recent years.

In order to reach fusion reactor conditions of high temperature, auxiliary heating of some form is needed. Two important forms of this, neutral beam injection (NBI) and ion cyclotron range of frequency (ICRF) heating, employ energetic ions to heat the plasma. In addition, fusion reactor plasmas will produce quantities of 3.5 MeV alpha particles. For all these energetic ions, whether from NBI, ICRF heating, or fusion reactions, it is desirable that they be well confined in the plasma. If they are not, then their energy is lost from the plasma, meaning that the efficiency of heating is lowered. Also, large or concentrated fast ion losses have the potential to damage the first wall of the device, possibly forcing lengthy repairs. For these reasons, it is valuable to understand the confinement and loss of energetic ions in helical plasma systems.

The Compact Helical System (CHS)[2] is a low aspect ratio heliotron whose vacuum vessel has a major radius of 100 cm, an average minor radius of 20 cm, and a maximum magnetic field on axis of 2 T. The helical winding is l=2, and has 8 field periods toroidally. Plasmas have R_{ax}=88.8—101.6 cm, line averaged density of n_e=1–4x10^{13} cm^{-3}, T_e=300 eV, and T_i=400 eV. The plasma in CHS may be formed either by electron cyclotron heating (ECH) or by ion Bernstein waves (IBWs). There are two neutral beam injectors on CHS, each capable of injecting ~1 MW of 40 keV H. The two beam lines, for the experiments described here, were oppositely directed: one injected in the direction of the magnetic field, and the other injected in the direction opposite to the field. The data in this paper was all taken with only coinjection. For all cases, except Fig. 10, the beam was injected with a tangency radius of 87 cm. In addition, the results reported here are for discharges with minimal levels of MHD activity as determined from magnetic pickup coils external to the plasma.

The work reported here consisted of scans of plasma parameters to find how these parameters influenced the beam ion loss rate. Section II describes the diagnostic used to detect lost beam ions. Section III describes beam ion orbit geometry and orbit calculations. Sec. IV describes the experimental observations and Sec. V presents conclusions and suggestions of directions for future work.

II. Beam Ion Loss Diagnostic

Beam ion loss from CHS was measured using a scintillator probe[3] of the type originated on TFTR.[4-6] The probe consists of a metal box, on one side of which are mounted two apertures, as shown in Fig. 1. The probe typically sits near the wall of CHS. Some beam ions are on orbits that transit both apertures of the probe. These ions strike the scintillator at a position determined by their gyroradius and pitch angle. Light produced from the fast ions striking the scintillator is collected by a lens in the probe assembly, and focused outside the vacuum. There, the light is shared between two detectors. The first detector consists of a microchannel plate image intensifier and attached CCD camera. This records several images of the light pattern on the scintillator over the course of NBI into a CHS discharge (~100 ms NBI duration and 33 ms video frame widths). The second detector was, for the first set of experiments, a single photomultiplier tube (PMT), whose output was digitized to give the total light intensity as a function of time during the discharge. Later, this detector was changed to a set of PMTs, coupled to the probe by an array of fiber optic cables.

The probe was initially constructed with a scintillator 25 x 25 mm, and a front aperture 0.8 mm high by 2 mm wide. The scintillator was ZnS(Ag) (P11), ~10 microns thick, deposited onto a quartz substrate. The line through the apertures and the center of the scintillator formed an angle of 35° from the machine's major radial line, and the plane of the scintillator was horizontal. This configuration is referred to as the "small" scintillator format. Later in the series of experiments reported here, the probe was rebuilt to accommodate a larger scintillator (32 x 32 mm), so that the large gyroradius portion of the distribution would not be cut off, and to put the apertures at an angle of 45° to the machine major radius line, in order to view lost particles at lower pitch angles. In addition, the front aperture was reduced to 0.5 x 2 mm to improve the resolution in gyroradius. Furthermore, a small light bulb was mounted on the inside of the probe shaft to illuminate the scintillator for position calibration in the camera field of view. Finally, the scintillator was deposited on an aluminum-coated quartz substrate, and a contact wire

installed so that the beam ion current collected by the scintillator could be measured external to the probe.[7] This latter configuration of the probe is referred to as the "large" scintillator format.

The probe was inserted into a port on top of the CHS device, located at R=120 cm, at a toroidal angle where the elliptical cross-section of the plasma had its major axis horizontal. The probe could be moved vertically, to measure the loss at different positions and to allow for its removal from the vacuum vessel. All measurements reported here are with the tip of the probe at 12 cm above the CHS midplane. A top view of the neutral beam injectors and probe location is shown in Fig. 2. While the present work focuses on observations of losses to this probe during discharges that are MHD quiescent, other work has investigated the characteristics of MHD related losses from CHS.[8-10] Similarly, characteristics of fast ion loss from the TJ-II stellarator have been reported in Ref. 11. A description of fast ion losses from the W7-AS stellarator is contained in Ref. 12.

III. Beam Ion Orbit Characteristics & Modeling

There are four general classes of particle orbits in the heliotron/torsatron geometry.[13, 14] These are, in order of increasing pitch angle (increasingly perpendicular velocity): passing, transition, banana, and helically trapped. Particles on passing orbits have a toroidal velocity that is always oriented in the same sense–either clockwise or counterclockwise. Such an orbit, for an ion in CHS, is depicted in Fig. 3. Particles on banana orbits experience a toroidal reflection at two points in their orbit, resulting in an orbit whose projection into the (R, Z) plane is banana-shaped. Such an ion orbit in CHS is depicted in Fig. 4. Transition orbits lie, in pitch angle, between passing and banana orbits, and have toroidal reflection points at irregular intervals. They behave somewhat stochastically, and have a large "orbit deviation," i.e. the particle can move in minor radius a significant distance from its initial position. One such beam ion orbit in CHS is depicted in Fig. 5. Helically trapped particles have a sufficiently high pitch angle that they experience magnetic reflection when they approach the nearest helical coil, and are therefore trapped between adjacent helical coils. A typical orbit of this sort is shown in Fig. 6.

Several characteristics of a particle's orbit determine whether it will be likely to strike the wall. These are the orbit deviation, the gyroradius, and the proximity of the starting point of the wall. In cases where the ratio of gyroradius to system size is small, the gyroradius may have negligible effect on whether the particle is lost. However, for 40 keV H beam ions in CHS, the gyroradius is a significant fraction of the minor radius: with R_{ax}=94.9 cm and B=0.9 T on axis, B near the plasma edge is ~0.65 T; beam ions at the magnetic axis will have a pitch angle of 23.5° ($\chi=\arccos(v_{\parallel}/v)$) and a gyroradius at the edge of 1.8 cm. Since the average minor radius of the CHS plasma is ~20 cm, $\rho/a\sim0.1$. If the pitch angle becomes more perpendicular, then this parameter can be several times larger, e.g. 1.9 times larger for the typical observed loss pitch angle of 50°. The orbit deviation for such energetic particles in CHS can also be large.

Beam ion orbits in CHS were modeled with a version of the Lorentz orbit code used previously at TFTR, PLT, and DIII-D.[15] This code was modified to incorporate the non-axisymmetric CHS magnetic field structure, and the CHS vessel wall structure. This code integrates numerically the Lorentz force law, and so gives the complete trajectory of the particle, including gyromotion. Because of the large ratio of gyroradius to minor radius, and because of the somewhat complex geometry of the vessel

wall, calculation of the complete gyromotion of the particle is more useful for comparison with experimental results than is a guiding center calculation.

This Lorentz orbit code used does have significant limitations. The code presently incorporates only the vxB term of the Lorentz force law, and does not include any electric field terms. Some CHS discharges show factor-of-two changes in the beam ion loss rate when ECH is applied. These changes may arise from alterations in the radial electric field profile inside the plasma, or may be the result of ECH-related changes in the density profile, which affects the beam deposition profile. Alternatively, the changes may arise from a combination of these effects. In general, global beam ion loss and local loss at the detector depend sensitively upon where in the plasma the particles become ionized. For most of the discussion in this paper, we have computed only individual particle orbits for the purpose of understanding the topology of orbits in different ranges of pitch angle at the detector, and we have ignored the question of beam deposition and the relative abundance of particles at different pitch angles at the detector. However, near the end of this work, we show a few results of an orbit model that includes the beam deposition profile.

IV. Experimental Results

A. Total Loss Rate Measurements

In this section of the paper, we describe the total loss rate of beam ions to the probe under various plasma conditions. These measurements come from the PMT that measures the total light produced by beam ions striking the scintillator. Unless otherwise noted, the data in this work were taken with B_T=0.9 T on axis, R_{ax}=94.9 cm, and a line averaged electron density of $n_e=2.5\text{x}10^{13}$ cm^{-3}.

The first test of the functionality of the probe on CHS was to measure the loss rate dependence upon the direction of the magnetic field. [3] Two discharges were formed, identical except that the direction of the magnetic field was clockwise (as seen from above) in one, and counterclockwise in the other. In the case of clockwise magnetic field, ions drift downward and away from the probe, and no beam ion loss signal was seen. When the direction of the field was reversed, beam ion loss was detected, and the PMT signal coincided in time with NBI. This result is depicted in Fig. 7. The PMT signal showed no correlation with H_α light from the plasma, indicating that the PMT signal was not simply due to plasma light leakage into the probe.

Figure 8 displays the total loss rate to the probe as the major radius of the magnetic axis of the plasma is varied. The detected loss rate increases exponentially as the plasma is moved outward in major radius. The e-folding distance for this increase is ~1.8 cm. Since the process of moving the plasma outward in minor radius moves it closer to the probe, it is not surprising that the loss rate increases. Particles on transition orbits behave approximately as though they are making stochastic steps inward and outward in minor radius. In that sense, they are diffusing outward. In the presence of an obstacle (some part of the CHS vessel wall, perhaps), the scrape-off profile will be exponentially decaying, and that may result in the response seen in Fig. 8. A study of this behavior for stochastic toroidal field ripple diffusion of fusion products in TFTR noted a similar loss dependence with position.[16, 17]

Figure 9 depicts the variation of the loss rate to the probe with plasma density. The data are well fit by a straight line. The linear dependence probably is the result of a linearly increasing rate of beam ionization over some range of minor radii where these loss orbits originate. The fact that the line extrapolates to a nonzero loss rate at zero density is not understood.

Figure 10 shows the variation in the total loss rate as a function of the beam injection angle (as measured at the point where the beam intersects the magnetic axis). The rate of loss increases by ~1.5 times as the beam injection angle varies from 6° to 34°. The population of beam ions will be at higher pitch angles with more perpendicular injection, and this will increase the number of ions on transition and banana orbits that may be lost to the probe. The variation in the loss rate might also be explained by the fact that the total path of the beam through the plasma is shorter in the case of more parallel injection, thus a smaller percentage of the beam particles will be ionized, producing a smaller population from which ions may be lost.

The total loss rate to the probe as a function the magnetic field on axis is shown in Fig. 11. The loss diminishes rapidly as the field increases above 0.9 T. This tendency arises because the poloidal field is also increasing, and the orbit deviation tends to scale inversely with the poloidal field strength. The gyroradius of the affected particles is also decreasing, also contributing to their reduced loss rate as B increases. The slope of the loss rate versus B_T is much flatter for fields above 0.9 T, indicating a less pronounced increase in confinement of beam ions as the field increases above this point.

CHS is equipped with an ion Bernstein wave (IBW) antenna that can be moved radially inward and outward. It is possible to move it far enough inward to intercept beam ion orbits under the standard conditions chosen for this experiment. Figure 12 presents the total loss rate as a function of the antenna position, showing a factor of ~8 variation of the loss rate over the 10 cm available range of antenna motion.

B. Pitch Angle and Gyroradius Measurements

The combination of the aperture arrangement of the probe and the magnetic field of the CHS device cause the probe to function as a sort of magnetic spectrometer, dispersing beam ion strike points across the scintillator according to their gyroradius and pitch angle. The light pattern produced by the beam ions striking the scintillator was imaged by a CCD camera, as described in Sec. II. The images were recorded and then digitized, enabling computational analysis to determine the distribution of the loss in pitch angle and gyroradius.

To generate the mapping between position on the scintillator and the corresponding gyroradius and pitch angle of the lost beam ions, a numerical model of the detector aperture, scintillator, and local magnetic field geometry, previously developed for detectors on TFTR.[4], was used. This simulation uses a Monte Carlo technique, launching numerous particles at a fixed pitch angle and gyroradius from positions distributed across the front aperture. The strike points of these particles on the scintillator are computed, and the centroid of the strike points is tabulated. The calculation is repeated for discrete values of pitch angle and gyroradius over the range of detection, and the grid of centroid points thus computed is used to interpret the image data. Note that the following conventions are adopted in this

paper: the pitch angle is defined by $\chi=\arccos(v_{\parallel}/v)$ and the "gyroradius" is defined to be $\rho=(2mE)^{1/2}/qB$ This definition of gyroradius makes it independent of pitch angle and a measure of the particle's energy only (at constant B).
From this computed detector grid and the position of the scintillator within the CCD camera image, a 2D polynomial is fit to define a coordinate transformation from Cartesian coordinates in the CCD camera image to (ρ, χ) centroid coordinates.

A typical image from the CCD camera is shown in Fig. 13. This data is from a discharge with R_{ax}=94.9 cm, and B_0=0.75 T, taken with the small scintillator. The image is shown as contours of constant brightness, overlaid with the computed centroid grid for this condition. This image shows losses that appear as 3 categories or spots in the image, labeled I, II, & III in the figure. The Category I loss is typically the strongest, and appears along a line of constant pitch angle between 45° and 50°, with a width approximately equal to the characteristic broadening introduced by the aperture set. At some plasma major radii, it vanishes when the magnetic field strength exceeds a certain critical value. Category II losses appear at a higher pitch angle than do Category I losses, typically between 60° and 70°. Category II losses have been observed over the full range of B scanned (0.75 T to 1.8 T), but are sometimes very much dimmer than the Category I losses. Category III losses appear at a pitch angle near but below that of Category I losses. This loss can appear as a wide single spot, or is sometimes divided into several narrow arcs, akin to Category I losses. Subsequent sections of the paper will present data on how the characteristics of these losses vary with plasma parameters.

Figure 14 shows a set of camera images taken with the same magnetic configuration as that in Fig. 13, but with differing angles of beam injection. Note that the loss features in this image are in the same positions regardless of the injection angle, indicating that they are strictly a function of the orbit topologies in this particular magnetic equilibrium and are not a function of exactly how the beam injection populates those orbits.

Figure 15 displays the complete gyroradius and pitch angle distributions at the probe for R_{ax}=94.9 cm as B_T is varied. The Category I loss is seen to move to lower pitch angle as B_T is increased, and it disappears entirely when B_T>1.3 T. While it exists, however, it maintains its narrow extent in pitch angle.

C. Variation of the Loss Pitch Angle and Gyroradius with Plasma Parameters

1. Category I Loss Characteristics

Figure 16 shows the gyroradius distribution from a discharge at standard conditions, taken with the small version of the probe. This gyroradius distribution has been produced by integrating in pitch angle from 47° to 53°, to encompass just the Category I loss. Given the magnetic field strength at the probe position in this condition, 40 keV H ions would have a gyroradius of ~4 cm. This is a marked departure from the peak gyroradius centroid value observed, which is 5.5 cm. To understand this observation, it must be noted that the gas feed to the neutral beam injector contained ~1% deuterium for this shot. If one computes 40 keV H orbits coming to the scintillator probe under this condition, it is found that they all intersect the vessel wall within a short distance the probe. This means that no injected H ions can actually be detected under this condition. Interestingly, though, if one computes the orbits of 40 keV deuterons in the same fashion, they do not collide with the vessel walls enroute to the probe. The

detector modeling code previously mentioned, when run with for 40 keV D ions under these conditions, predicts a gyroradius centroid distribution at the detector that peaks at 5.5 cm, in good agreement with the measurement. Consequently we infer that this is a loss of D beam ions in this case.

Figure 17 displays the pitch angle distribution for the same shot as in Fig. 16. The peak at 49° is due to this Category I loss, and its shape is matched by a model distribution centered at 48.5° when the signal is convolved with a Gaussian of width 0.5 mm to simulate broadening in the optics of the detector.

To learn more about the nature of the Category I loss, a scan of the magnetic field strength was performed. Figure 18 shows the mean gyroradius centroid of the Category I loss spot as a function of B_T, for R_{ax}=94.9 cm. Note that this type of loss is not seen when B_T>1.3 T. Included are data from B_T scans during two different experiments. The results are in good agreement with each other, and the best least-squares fit to a power law form is $\rho \propto B^{-1.05}$, indicating that the loss is at constant energy as B varies. The mean energy is consistent with the 38-40 keV beam injection energy, implying that the loss occurs rapidly compared to the beam ion slowing down time, ~12 ms in these plasmas.

Figure 19 depicts the variation of the mean pitch angle of the Category I loss as a function of the plasma density. Within the error bars the pitch angle of loss is constant at 49.5° as the density increases from 0.5 to 2.6×10^{13} cm^{-3}. This constancy is expected, since changing the plasma density does not alter the magnetic geometry and, therefore, does not alter the topology of beam ion orbits.

Figure 20 presents the mean pitch angle of the Category I loss for the same B scans as shown in Fig. 14. The observed pitch angle changes by ~4° as the field was scanned from 0.75 T to 1.3 T. Also plotted is the range of pitch angles over which transition orbits exist at the detector. The limits of this range were determined by using the orbit code described in Sec. III to plot orbits over this narrow range of pitch angle, following them for ~3 toroidal transits starting from the probe aperture. Ions which underwent toroidal reflection at the very first magnetic field maximum they encountered were taken to be banana orbits—these invariably strike the vessel wall within a few tens of centimeters from the detector, and hence can have no appreciable source rate. If the particle was able to pass several field maxima before undergoing toroidal reflection, it was taken to be a transition orbit. Finally, if no toroidal reflections were observed within the ~3 toroidal transits computed, the particle was labeled as a passing particle. Within the errors of measurement, the pitch angles of this Category I loss overlap the range of pitch angles expected for transition orbit particles, leading us to identify the Category I loss mechanism as transition orbits. That the loss is relatively more intense than Category II or III losses is presumably due to the large orbit deviation of these orbits: they can originate nearer the center of the plasma, where the source rate of beam ions is much larger.

Figure 21 displays the measured Category I pitch angle as R_{ax} was varied, along with the pitch angle of transition orbit beam particles as determined by the method described in the preceding paragraph. The measured loss pitch angle is in all cases in good agreement with the transition orbit pitch angle.

The pitch angle and gyroradius of the Category I lost beam ions were also measured during the scan of the beam injection angle depicted in Figs. 8 and 14. The mean gyroradius centroid was constant within ±1.5% over the scan and corresponded to the gyroradius of injection-energy beam ions.

To learn more about how the wall position affected the loss measurements, data was taken during a position scan of the IBW antenna, which is located on the outer midplane of the vessel. Figure 22 displays the gyroradius centroid distributions (averaged over all pitch angles from 35°–80°), as measured by the large version of the probe, during the IBW antenna scan. The gyroradius distributions are essentially identical, regardless of the antenna position, and only the total amplitude of the loss has changed. This is consistent with the prompt nature of the loss, meaning the loss is comprised of injection energy particles that have not slowed down.

Figure 23 shows the pitch angle distributions of the loss during the IBW antenna position scan. Here, there is a component of the loss centered at a pitch angle of 45° which is much more strongly affected by the change in antenna position than is the loss at lower pitch angles. The reason for this preferential scrape-off of particles at 45° is not definitely known. We conjecture that this occurs because the transition orbits, which constitute the 45° peak, have a larger orbit deviation than do the passing orbits which produce the loss at lower pitch angles. Hence, the transitions orbits are scraped off more readily than are the lower pitch angle passing orbits.

2. Category II Losses

In this section, we describe the characteristics of the Category II loss which, as depicted in Fig. 13, occur at higher pitch angles than the Category I loss, typically 60°–65°. Figure 24 depicts the mean gyroradius centroid as a function of B. The best least-squares fit to this data is $\rho \propto B^{-0.903}$, indicating the loss is at an approximately constant energy. The mean gyroradius centroid is slightly lower than that observed for the Category I loss, but is still, within experimental errors, equal to the gyroradius centroid expected for injection energy particles.

Figure 25 displays the observed mean pitch angle of the Category II loss as a function of B. The mean pitch angle of the loss increases from 61.4° at B_T=0.75 T to 66.0° at 1.7 T. Unlike the Category I pitch angle, the pitch angle of this loss does not correspond to any special class of orbits; orbits at pitch angles above and below the pitch angle of this loss have very similar shapes, and all intersect the wall within a short distance from the probe. We conjecture that this loss arises from a small population of beam ions which are born on orbits which are immediately lost to the walls within a few tens of centimeters. If so, then the pitch angle range of the loss, which is considerably broader than that of the Category I loss, is determined by the combined effects of which orbits the detector is able to view and the range of minor radii over which beam particles ionize. The total intensity of this component of the loss is approximately constant over the range of B sampled.

Figure 26 shows the behavior of the mean pitch angle of this Category II loss as a function of the plasma density, at R_{ax}=94.9 cm and B_T=1.8 T. The pitch angle is observed to increase from ~63° to ~68° as the plasma density increases from 0.5×10^{19} m^{-3} to 5×10^{19} m^{-3}. The reason for this variation is unclear, and is counter-intuitive, since orbits at a pitch angle of 68° penetrate slightly closer to the magnetic axis of the plasma than do orbits at 63°. However, for higher density plasmas, more ionization should occur at a larger minor radius, implying that lower pitch angles should be observed at the detector. The mean gyroradius centroid was also measured during the density scan, and was found to be constant at ~2.4 cm, within the errors of measurement. This corresponds well with the injection energy of 40 keV.

3. Category III Losses

Figure 13 shows evidence of a loss at pitch angles below those of the Category I loss, in a range of pitch angles corresponding to passing orbits. These are presumably a class of orbits on which some beam ions are born, which intersect the wall. The data in Fig. 13 was taken with the small version of the probe, and it appears that some of the Category III loss data is missing, because the luminous spot extends beyond the edge of the scintillator. Only a slim handful of data was taken with the large version of the probe, so there is very little quantitative information about this loss. It sometimes appears as one or two narrow bands in pitch angle, something like the Category I loss. At other times, it appears over a broader range in pitch angle, as in Fig. 13. The reason for this is unclear.

VI. Orbit modeling with calculated beam deposition profiles

Thus far in this work, we have presented details of the beam ion loss distributions under various conditions and have shown that certain features of the pitch angle distributions correlate well with the boundaries between orbit classes in the magnetic equilibria considered. In this section, we attempt to take that effort a step further by incorporating a source term into the beam ion orbit following calculation. More specifically, orbits that reach the detector are integrated backward in time in the known magnetic equilibrium. At each step in the orbit, an incremental source strength is calculated. That source strength is taken to be a product of the deposition density of the beam at that position multiplied by a factor accounting for how closely the velocity of the particle at that step aligns with the direction of injection. The spatial deposition density is computed by a polynomial fit to a deposition profile computed separately by the H-FREYA code[18] for the discharge under study. The velocity vector alignment term is computed as $\exp(-\theta_{ba}^2/\theta_{b0}^2)$, where θ_{ba} is the angle between the beam injection direction and the particle's local velocity and θ_{b0} is the divergence angle of the CHS neutral beam injector, which is ~1.2°. The incremental source strength along an orbit is summed over the length of the orbit (typically until it intersects the wall) and is normalized to the total incremental source strength over all positions in the plasma and over all angles of deviation from the injection direction in order to provide a net detection efficiency for that particular orbit. By repeating this process over the full range of pitch angles received by the detector, it is possible to compute the expected pitch angle distribution at the detector and the total intensity at the detector. These quantities can then be compared with the measurements. Since there is no absolute calibration of the luminosity of the scintillator and camera system, the simplest method of comparing the modeling results with experiment is to show the relative loss rates in a parameter scan or the relative pitch angle distributions. Figure 27 shows the measured and modeled loss as a function of R_{ax}, with the measurements normalized to the calculated detection efficiency. The model agrees well with the variation of the measurement. Figure 28 compares the measured and modeled pitch angle distribution for R_{ax}=94.9 cm, B_T=0.9 T. Note that the measured pitch angle distribution shows a large peak at 50°, the position of the Category I loss for this condition. The modeled efficiency for various initial pitch angles is shown as open circles in this plot. Note the scatter of this data, which shows that the calculation is very sensitive to the initial conditions. In order to allow easier comparison by eye, a running average of the individual calculated efficiencies has also been plotted in this figure. Note that this running average peaks at ~42°, and has reached zero at 50°. This difference of 8° between the measured and predicted peak pitch angles is far larger than the accuracy of the detector (~0.5°) and it must be concluded that the model does not agree with the measurements.

VI. Discussion

The several categories of loss described herein all have the feature that the gyroradius of the loss matches that of the full energy injected ions. This means that whatever processes produce loss do so on a time scale short compared to the beam ion slowing down time. However, since the computational model described in the preceding section contains all the physics of prompt orbit loss but does not explain the observed pitch angle distribution, it must be concluded that the observed losses are not prompt loss. Given that the absolute sensitivity of the detector is unknown, it is possible that there could be some processes that generate losses of such a magnitude that modeled prompt loss is relatively small by comparison. Mechanisms such as collisional pitch angle scattering, error fields, low level MHD activity, plasma turbulence, and radial electric fields are possible candidates for additional loss processes that would result in pitch angle distributions different from what the model described here predicts. In particular, with respect to the last item, it was seen that the loss rate was altered during ECH, which is known to affect the radial electric field structure. Measurements on TJ-II[11] also indicate a change in beam ion loss rate during ECH. Given that the dominant feature of the loss signal is the loss of ions at the pitch angle of transition orbits, it seems possible that one or several of the processes listed above might move passing particles (presumably the dominant population of particles given the injection angle under normal conditions) onto transition orbits. Such a process could then produce a pitch angle distribution consistent with the observations. With regard to MHD activity, since the discharges selected for this work have a minimal level of activity evident on the external magnetic pickup coils, if the losses reported here are attributable to MHD, they must be due to modes which have their largest amplitudes in the core of the plasma with little or no amplitude at the edge.

VII. Conclusions and Directions for Future Work

The loss rate of neutral beam ions from CHS increases linearly with plasma density. The most pronounced losses observed by the fast ion loss probe on CHS are of beam ions on transition orbits. There also exist losses of passing particles, apparently from orbits that come to the CHS vessel wall. Losses of trapped particles at a pitch angle of ~65° were also observed. This pitch angle is well away from any boundaries in particle orbit space, and is therefore difficult to explain. A computational model of prompt loss from these plasmas is able to reproduce the variation of total loss with magnetic axis position, but predicts a different pitch angle distribution than that seen. From this, we conclude that additional loss processes are active beyond simple prompt orbit loss. Future investigations should try to determine which candidate processes are most likely or most important in producing the pitch angle distributions and loss rates seen.

Acknowledgements

One author, DSD, wishes to acknowledge the considerable hospitality shown by the staff of the National Insitute for Fusion Science during this work. The interest and support of Prof. A. Iiyoshi, Drs. K. Matsuoka, S. Okamura, and T. Watari of NIFS and Prof. R. Goldston of PPPL are greatly appreciated. This work supported by US DoE contract numbers DE-AC02-76CH03073 and DE-AC02-09CH11466.

References

[1] L. Spitzer, *Phys. Fluids* **1**, 253 (1958).
[2] K. Nishimura, *et al., Fusion Tech.* **17**, 86 (1990).
[3] D. S. Darrow, *et al., J. Plasma Fusion Res. SERIES* **1**, 362 (1998).
[4] S. J. Zweben, R. L. Boivin, M. Diesso, S. Hayes, H. W. Hendel, H. Park, J. D. Strachan, *Nucl. Fusion* **30**, 1551 (1990).
[5] D. S. Darrow, H. W. Herrmann, D. W. Johnson, R. J. Marsala, R. W. Palladino, S. J. Zweben, M. Tuszewski, *Rev. Sci. Instrum.* **66**, 476 (1995).
[6] D. S. Darrow, S. J. Zweben, H. W. Herrmann, *Fusion Engineering Design,* **34-5**, 53 (1997).
[7] D. S. Darrow, M. Isobe, T. Kondo, M. Sasao, and the CHS Group, *Rev. Sci. Instrum.* **70** (Part 2), 838 (1999).

[8] T. Kondo, M. Isobe, M. Sasao, D. S. Darrow, K. Toi, M. Takechi, G. Matsunaga, M. Osakabe, Y. Yoshimura, S. C. Takahashi, S. Nishimura, S. Okamura, K. Matsuoka, and the CHS Group, *Nucl. Fusion* **40**, 1575 (2000).
[9] K. Shinohara, M. Isobe, D. S. Darrow, *Rev. Sci. Instrum.* **77**, 10E521 (2006).
[10] M. Isobe, K. Toi, H. Matsushita, *et al*, *Nucl. Fusion* **46**, S918 (2006).
[11] D. Jiménez-Rey, B. Zurro, J. Guasp, M. Liniers, A. Baciero, M. García-Muñoz, A. Fernández, G. García, L. Rodriguez-Barquero, J. M. Fontdecaba, *Rev. Sci. Instrum.* **79**, 093511 (2008).
[12] A. Werner, A. Weller, D. S. Darrow, W7-AS Team, *Rev. Sci. Instrum.* **72**, 780 (2001).
[13] "The particle orbit in heliotrons," M. Wakatani, Chapter 6 in Stellarator and Heliotron Devices (International Series of Monographs on Physics) Oxford Univ. Press on Demand (1998/5/14), ISBN-10: 0195078314, ISBN-13: 978-0195078312.
[14] H.Sanuki, J. Todoroki and T. Kamimura, *Phys. Fluids B* **2** , 2155 (1990).
[15] J. Felt, *et al., Rev. Sci. Instrum.* **61**, 3262 (1990).
[16] R. L. Boivin, S. J. Zweben, and R. B. White, *Nucl. Fusion* **33**, 449 (1993).
[17] R. L. Boivin and S. J. Zweben, *Phys. Fluids B*, **5**, 1559 (1993).
[18] S. Murakami, *Trans. Fusion Technology* **27**, 256 (1995)

Figures

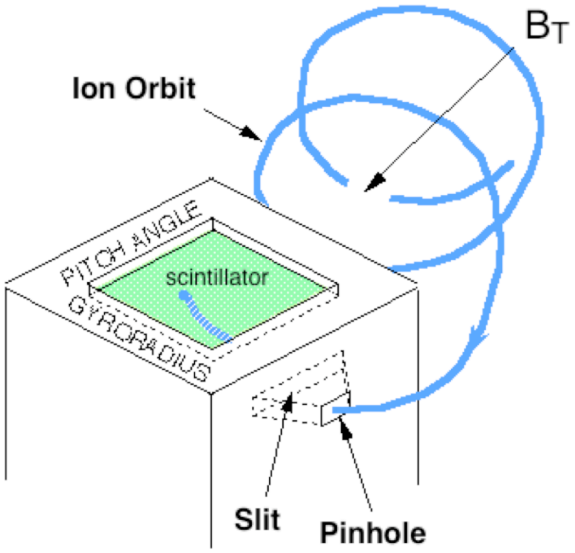

Figure 1: The geometric arrangement of an aperture pair inside the probe, the scintillator plate, and the confining magnetic field of the plasma act as a magnetic spectrometer, dispersing lost fast ions so that they strike the phosphor plate at a position determined by their gyroradius and pitch angle. An optical system viewing the scintillator plate allows the total luminosity vs. time to be recorded by a photomultiplier tube and the evolution of the luminous pattern in time to be captured by a video camera.

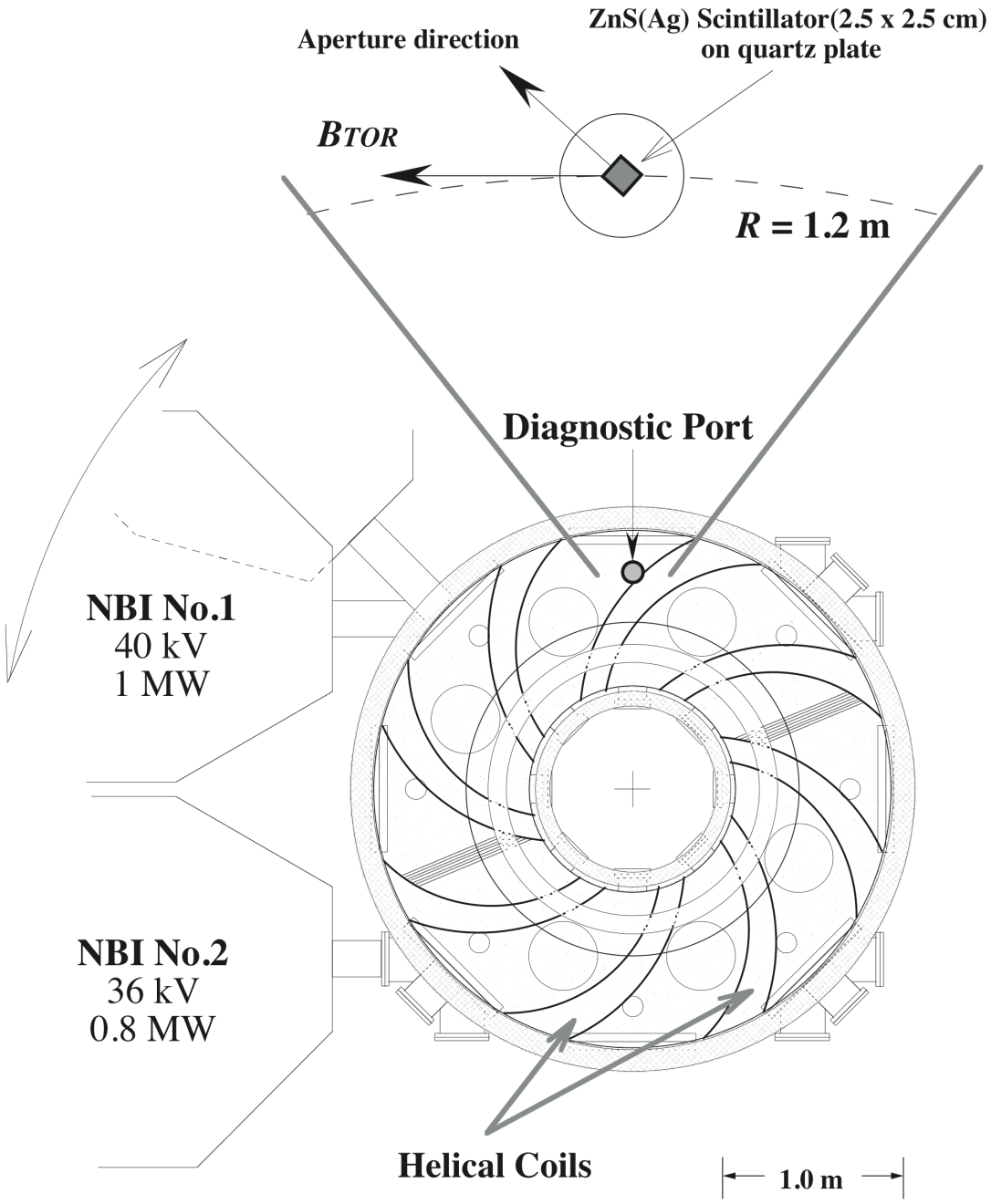

Figure 2: Top view of CHS showing the positions of the neutral beam injectors and the scintillator probe, along with the orientation of the entrance aperture of the probe. Only NBI No. 1 was used for the experiments described herein.

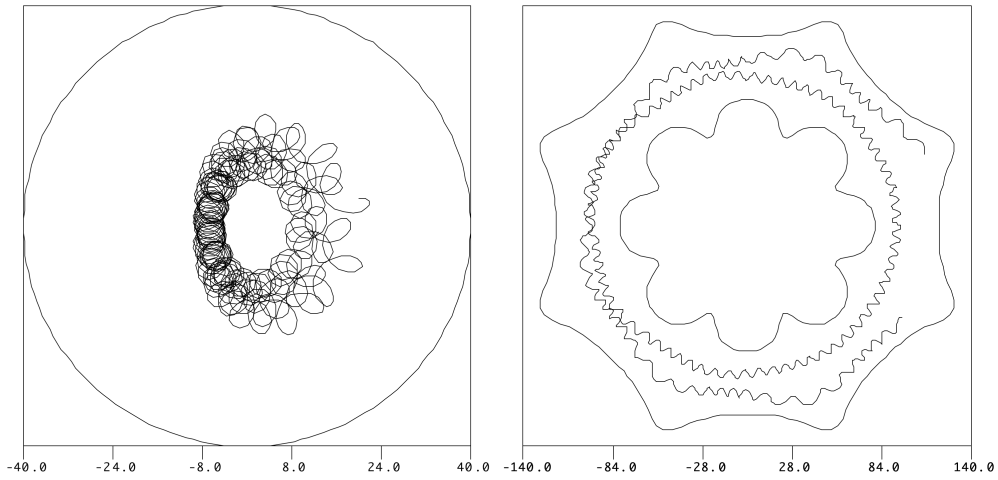

Figure 3: Plot of a passing 40 keV neutral beam injected proton orbit in CHS. The circle in this plot has a radius of 40 cm and thus will be tangent to the vessel elliptical cross section at any toroidal angle. The left hand plot shows all steps in the orbit projected into a plane at a single value of toroidal angle. The right hand plot shows all the steps of the orbit projected into the midplane (Z=0). The inner and outer curves are the position of the vacuum vessel surface in the midplane.

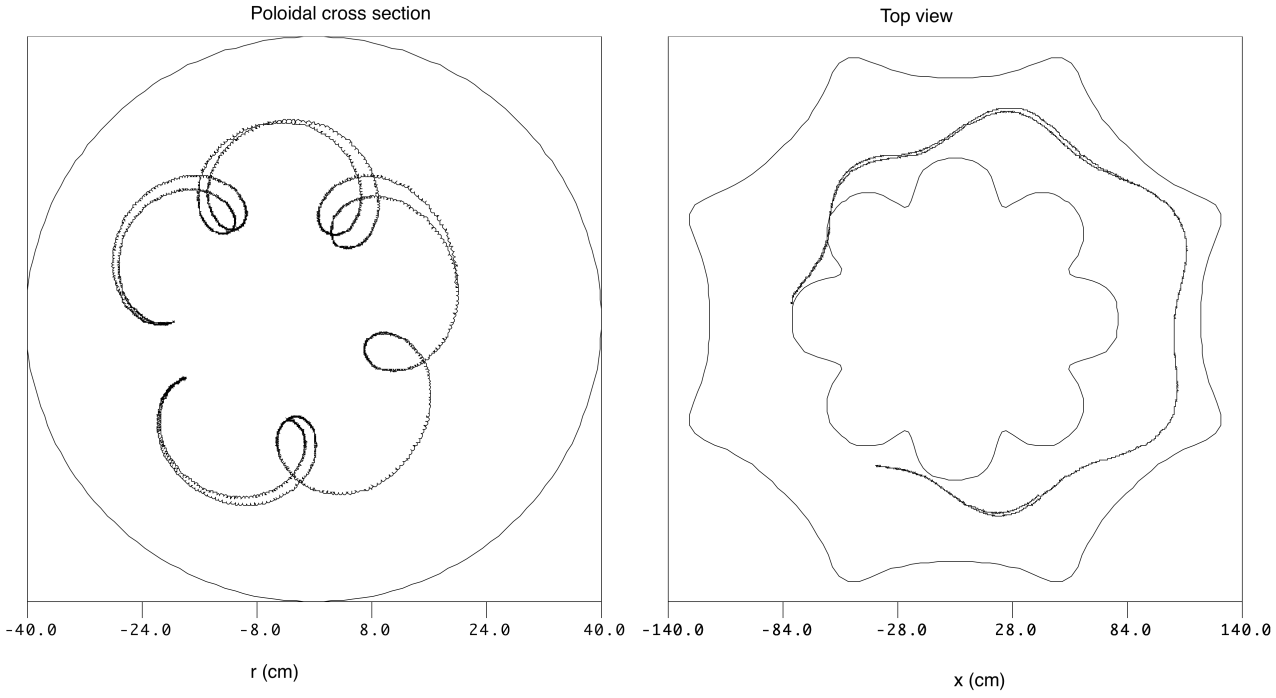

Figure 4: Plot of a 100 eV toroidally trapped proton orbit in CHS. Note, in the top view, the two points at which the orbit stops, then turns to move in the opposite direction toroiodally. Note also that, for purposes of clarity of depiction, this is the orbit of a relatively low energy ion and not one of a neutral beam ion in CHS.

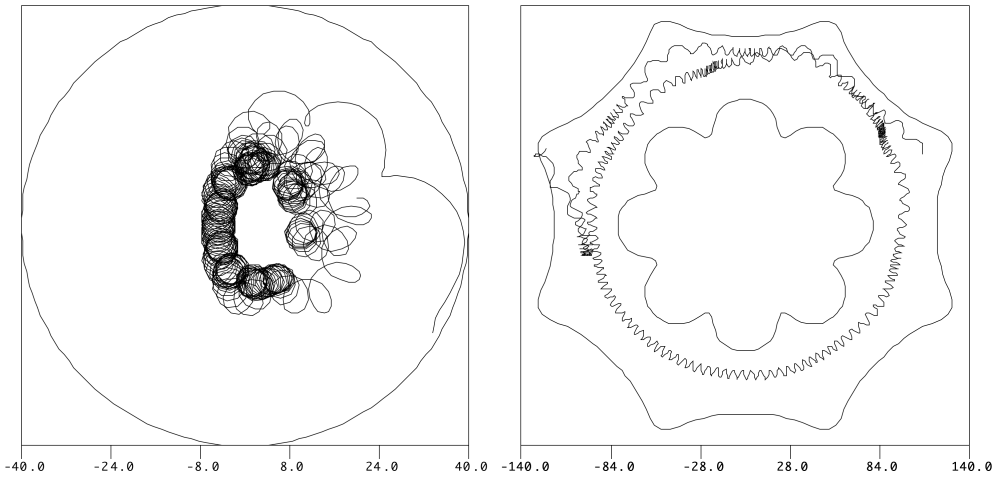

Figure 5: Plot of a 40 keV proton on a transition orbit in CHS. Note the several positions (seen as darker sections of the orbit in the top view) where the particle has predominantly perpendicular velocity and hence is close to undergoing magnetic mirroring. These positions do not appear to be regularly spaced, indicative of the somewhat stochastic nature of these orbits, which contributes to their propensity to be lost.

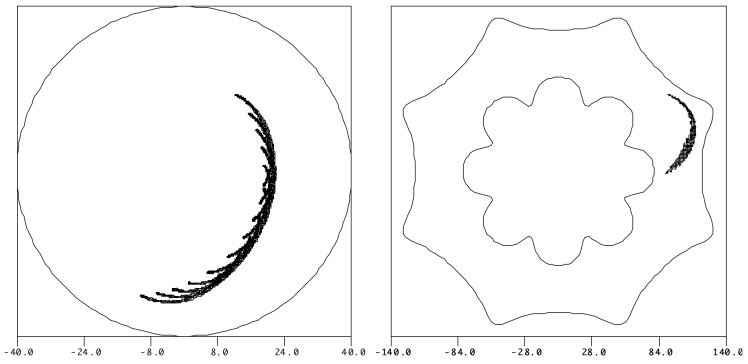

Figure 6: Plot of a helically trapped 100 eV proton orbit in CHS. Note the repeated reflections as the particle is trapped between adjacent windings of the helical coil. Note again that this is a particle with an energy well below that of a beam ion for the sake of clarity in depiction of the orbit.

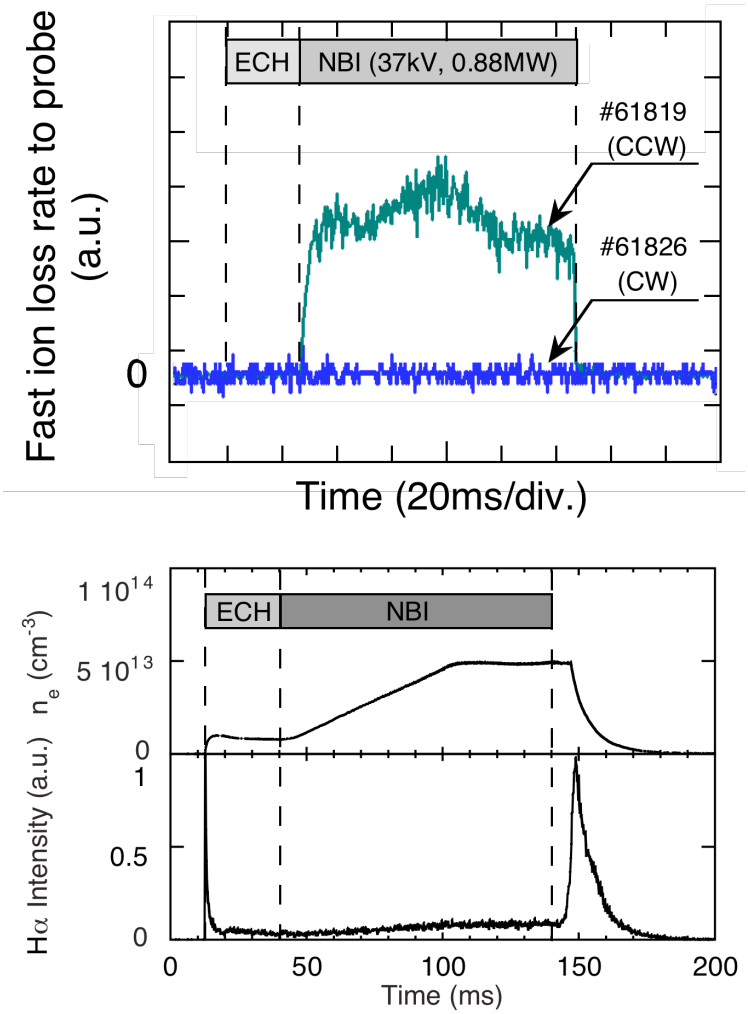

Figure 7: (a) Time history of the total scintillator light, as measured by the PMT, for the toroidal field pointing clockwise as seen from above (in which condition ions undergo a grad-B drift downward, away from the probe), and counterclockwise (where ions drift upward from the plasma, toward the probe.) The fact that light is seen only when the magnetic field is oriented such that ions will drift toward the probe from the plasma and the fact that the light is seen only when the neutral beams are injecting indicates that beam ion loss is being measured.
(b) Time history of the H_α light for the same case of counterclockwise magnetic field direction as shown in part (a). The fact that the PMT time history does not follow the H_α light intensity in time verifies that the PMT measurement is not a result of leakage of plasma light into the probe.

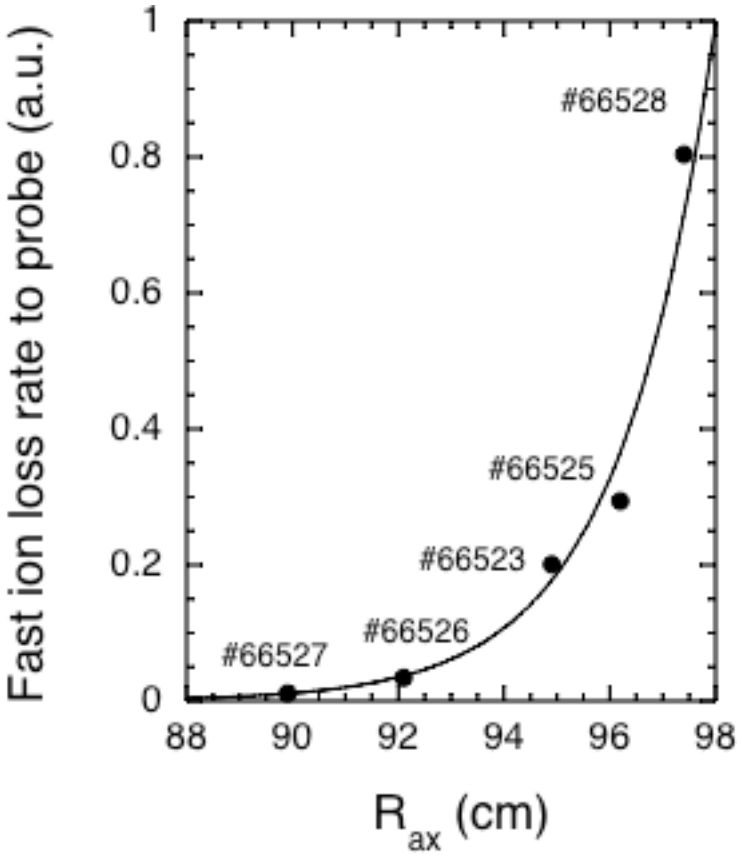

Figure 8: Total beam ion loss rate as a function of the magnetic axis position. The measurements are the solid circles. The loss rate is reasonably well fit by the exponential function shown in the solid line.

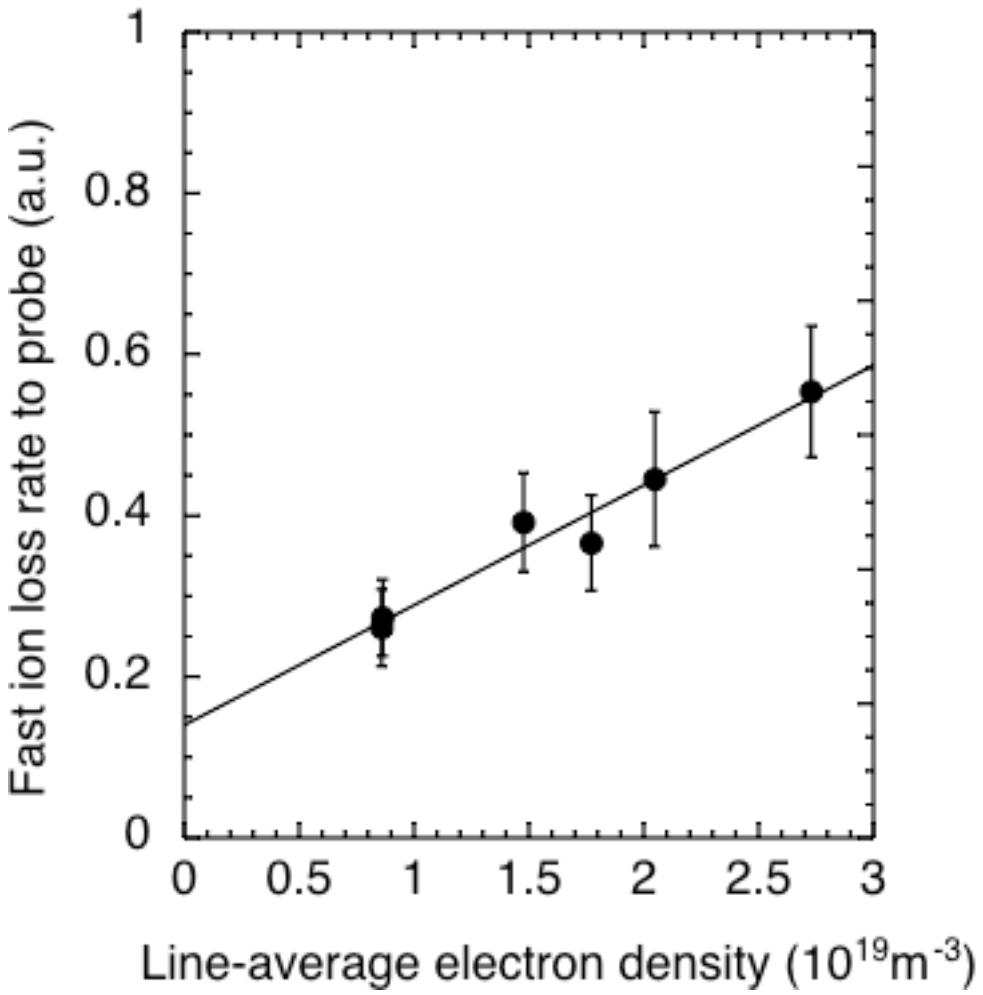

Figure 9: Total beam ion loss rate as a function of line average electron density for R_{ax}=94.9 cm and B_T=0.9 T. The loss rate increases linearly with the line average density.

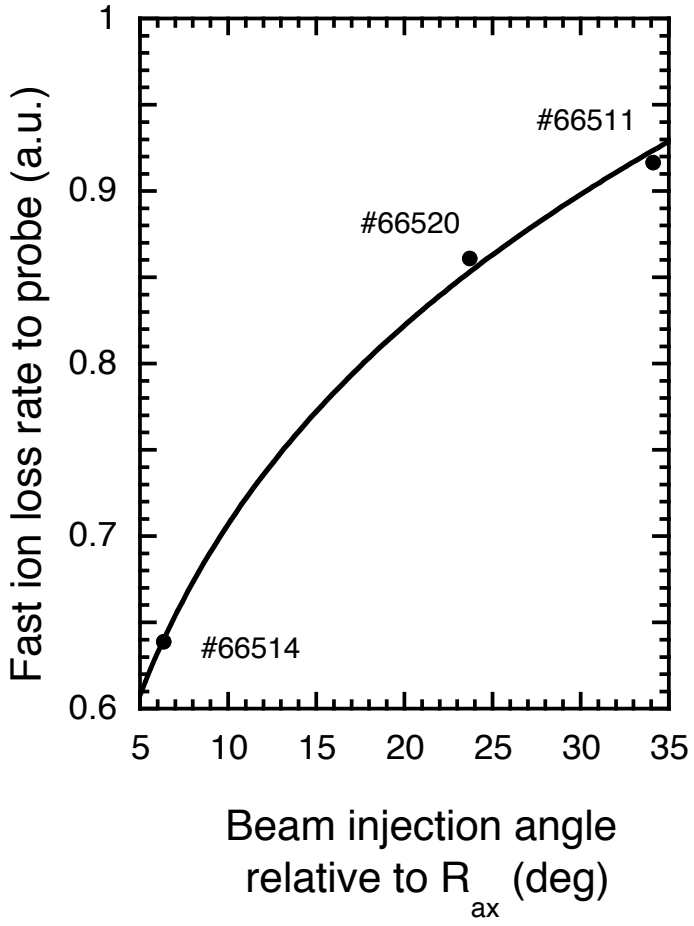

Figure 10: Total beam ion loss rate as a function of beam injection angle. The angle stated is the angle between the centerline of the beam and the magnetic axis at the point where the beam centerline crosses the axis. The curve shown is the best least squares fit power law form to this data. The result is that the fast ion loss varies as the angle raised to the power 0.22.

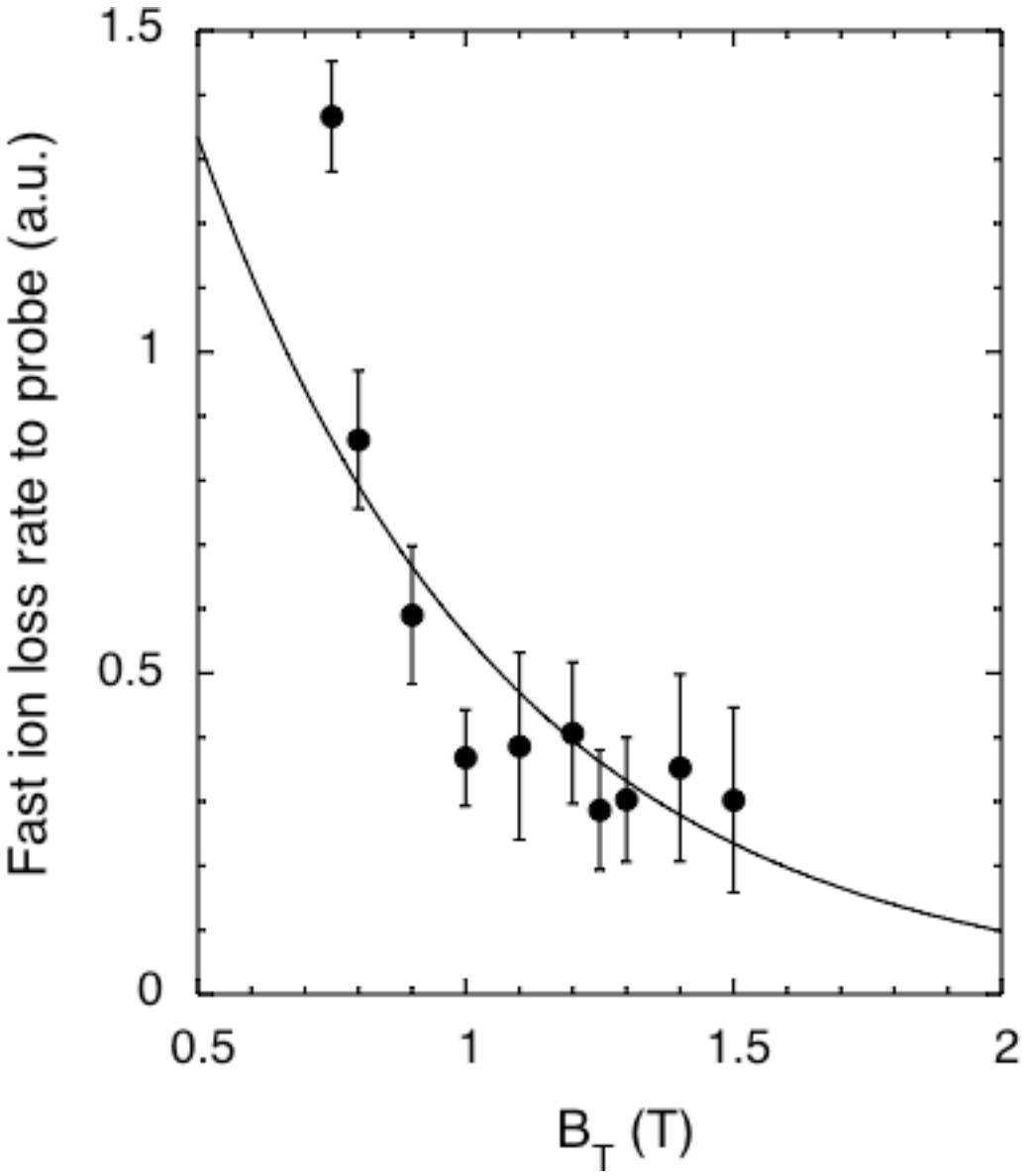

Figure 11: Total beam ion loss rate as a function of toroidal field for Rax=94.9 cm The fitted curve in the figure is of an exponential form, indicating a very rapid reduction in loss rate as the field increases. It has an e-folding scale length of 0.58 T.

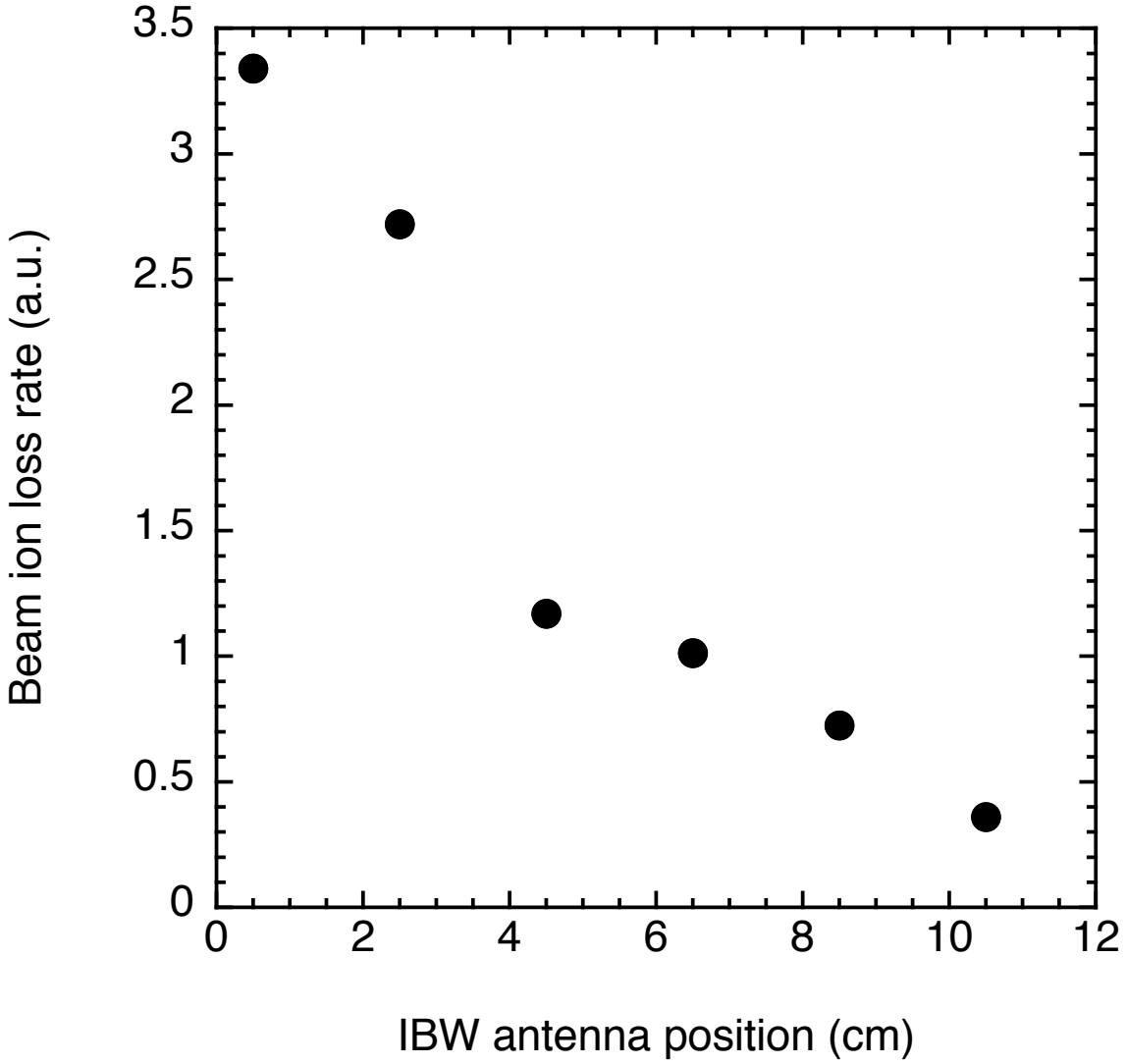

Figure 12: Total neutral beam ion loss rate as a function of the IBW antenna radial position. The loss rate decreases by a factor of ~8 as the antenna is moved inward over a range of ~10 cm.

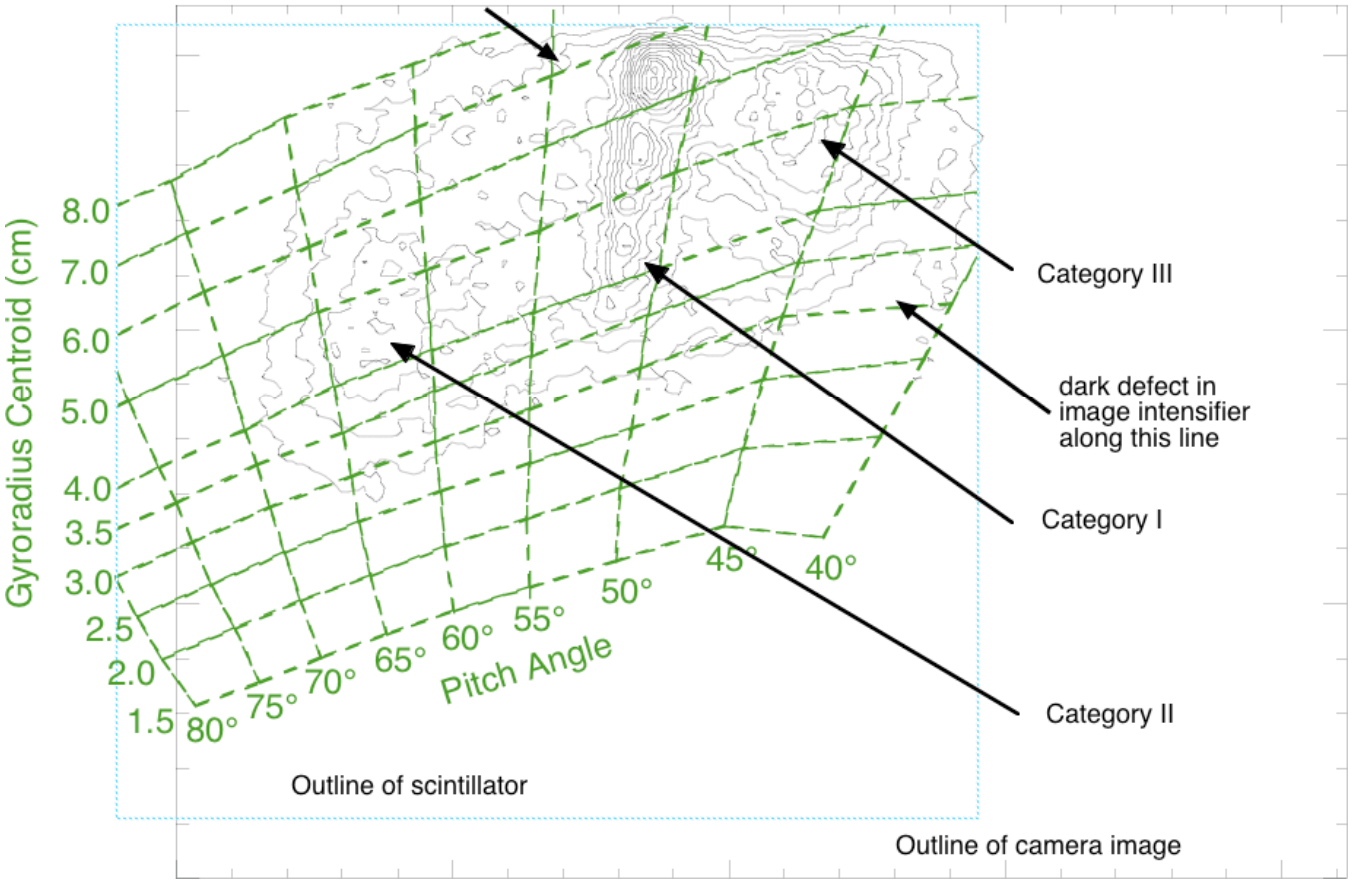

Figure 13: Contour plot of the light intensity from a scintillator image for R_{ax}=94.9 cm, B_T=0.75 T (Shot 67420, frame 3) with superimposed pitch angle and gyroradius grid. Note that there is an instrumental artifact in the data produced by a diagonal black line on the camera's image intensifier. This black line suppresses the apparent intensity over a narrow region of each image. The line's position is delineated by arrows in the figure. The loss exhibits three main spots, as labeled. These are: Category I ($50° \le \chi \le 55°$), Category II ($55° \le \chi$), and Category III ($\chi \le 50°$). The exact pitch angle ranges associated with each category of loss vary with the magnetic configuration of the discharge, but their general characteristics are preserved, as can be seen in some ensuing figures.

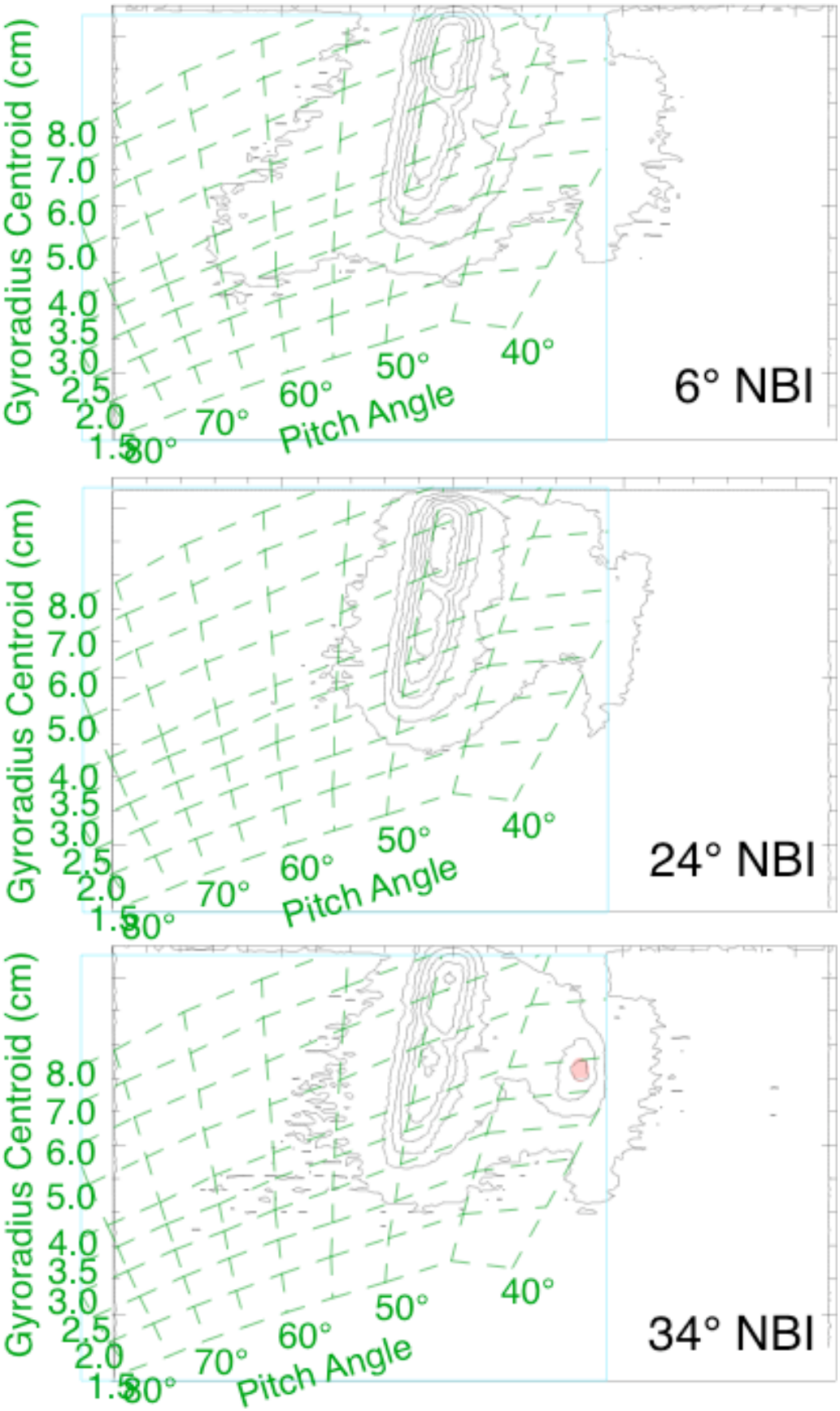
Gyroradius Centroid (cm)
8.0
7.0
6.0
5.0
4.0
3.5
3.0
2.5
2.0
1.5
80°
70°
60°
50°
40°
Pitch Angle
6° NBI
Gyroradius Centroid (cm)
8.0
7.0
6.0
5.0
4.0
3.5
3.0
2.5
2.0
1.5
80°
70°
60°
50°
40°
Pitch Angle
24° NBI
Gyroradius Centroid (cm)
8.0
7.0
6.0
5.0
4.0
3.5
3.0
2.5
2.0
1.5
80°
70°
60°
50°
40°
Pitch Angle
34° NBI

Figure 14: Contour plots of light intensity from scintillator images with R_{ax}=94.9 cm, B_T=0.9 T with beam injection angles of 6°, 24°, and 34° with respect to the magnetic axis (neutral beam tangency radii of R_{tan}=94, 87, and 80 cm, respectively). Note that the same categories of loss appear at the same pitch angle ranges, since the topology of lost and confined orbits is determined by the magnetic equilibrium alone. Data is from shot 66514 for 6°, 66520 for 24°, and 66511 for 34°)

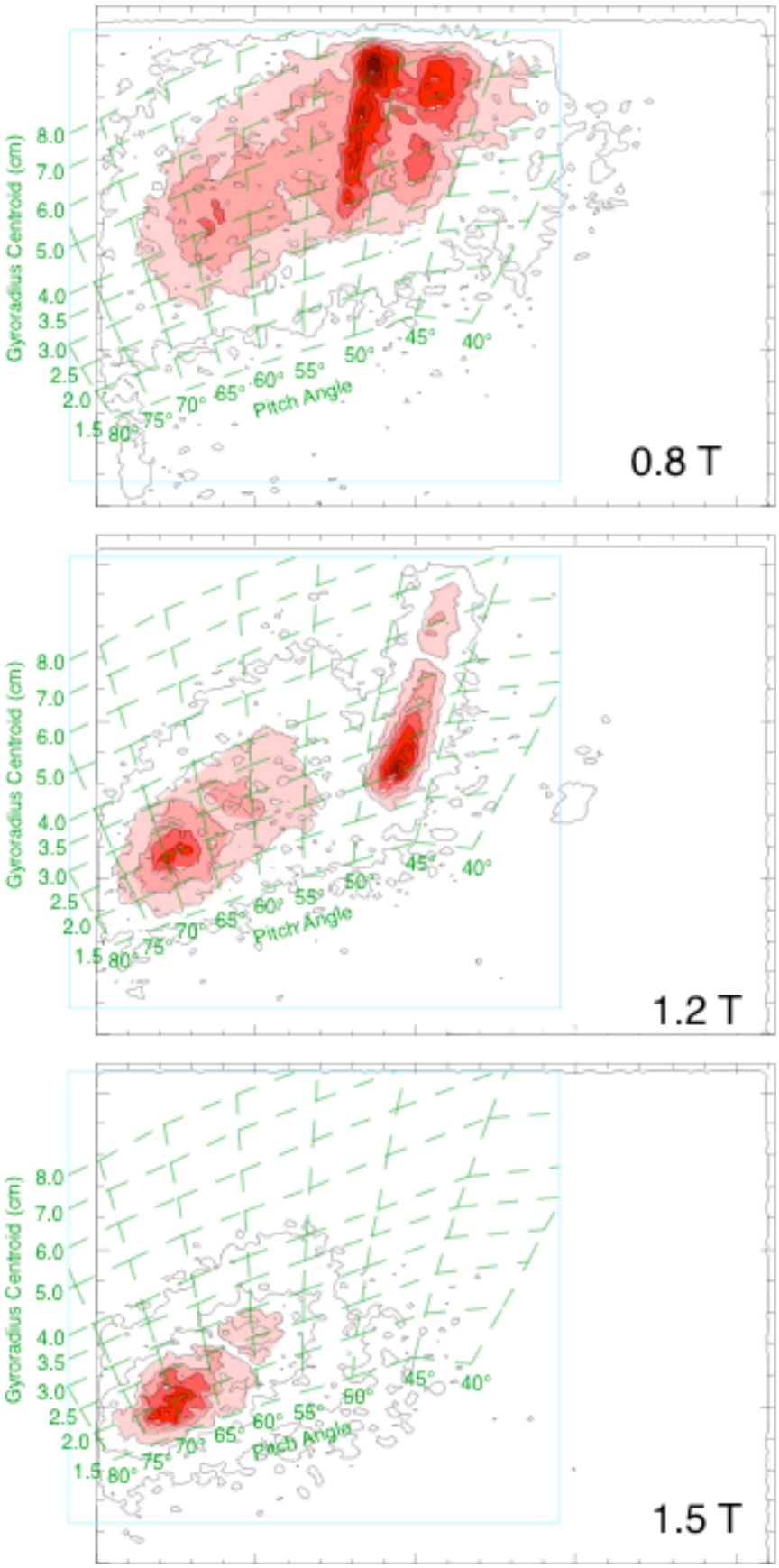
Gyroradius Centroid (cm)
8.0
7.0
6.0
5.0
4.0
3.5
3.0
2.5
2.0
1.5
80°
75°
70°
65°
60°
55°
50°
45°
40°
Pitch Angle
0.8 T
Gyroradius Centroid (cm)
8.0
7.0
6.0
5.0
4.0
3.5
3.0
2.5
2.0
1.5
80°
75°
70°
65°
60°
55°
50°
45°
40°
Pitch Angle
1.2 T
Gyroradius Centroid (cm)
8.0
7.0
6.0
5.0
4.0
3.5
3.0
2.5
2.0
1.5
80°
75°
70°
65°
60°
55°
50°
45°
40°
Pitch Angle
1.5 T

Figure 15: Contour plots of light intensity from scintillator images for R_{ax}=94.9 cm, B_T=0.8, 1.2, and 1.5 T with superimposed pitch angle and gyroradius grids. From these plots, it can be seen that the Category I loss retains its narrow extent in pitch angle over the range of fields for which it is present. It can also bee seen that the Category I loss disappears entirely in the 1.5 T case, as does the Category III loss. In contrast, though, the Category II loss at higher pitch angle is present at all values of B_T shown.

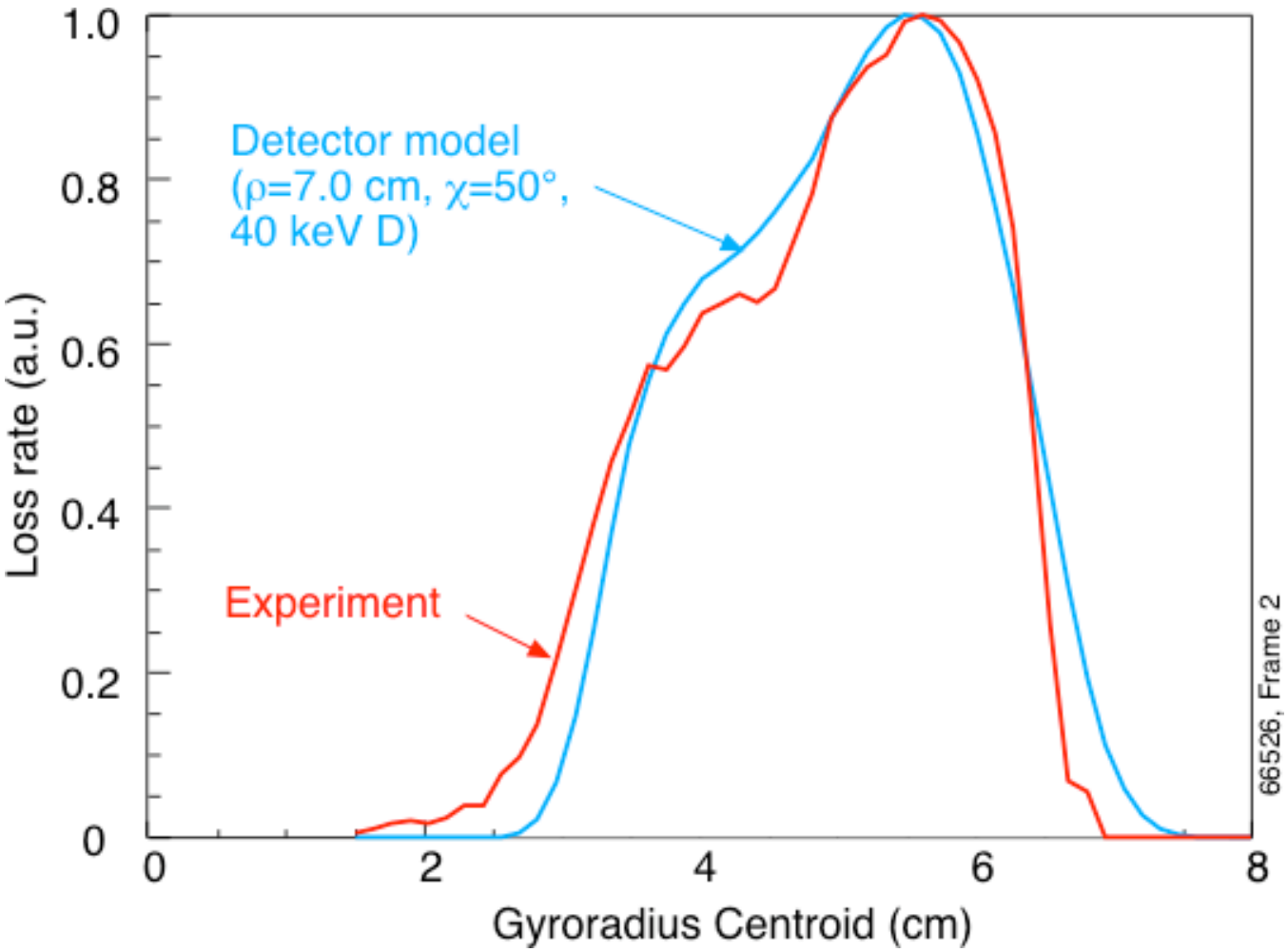

Figure 16: Measured and modeled gyroradius distribution at the detector for R_{ax}=92.1 cm, B_T=0.9 T (shot 66526, frame 2). The measured gyroradius centroid distribution does not agree with that expected for 40 keV H ions in this magnetic equilibrium. However, as described in the text, deuterium was also injected in this condition. All the H ion orbits strike the vessel wall before reaching the detector position. However, 40 keV D ions are able to reach the detector in this equilibrium, and the modeled gyroradius centroid distribution for 40 keV D ions, also shown here, is in good agreement with that observed.

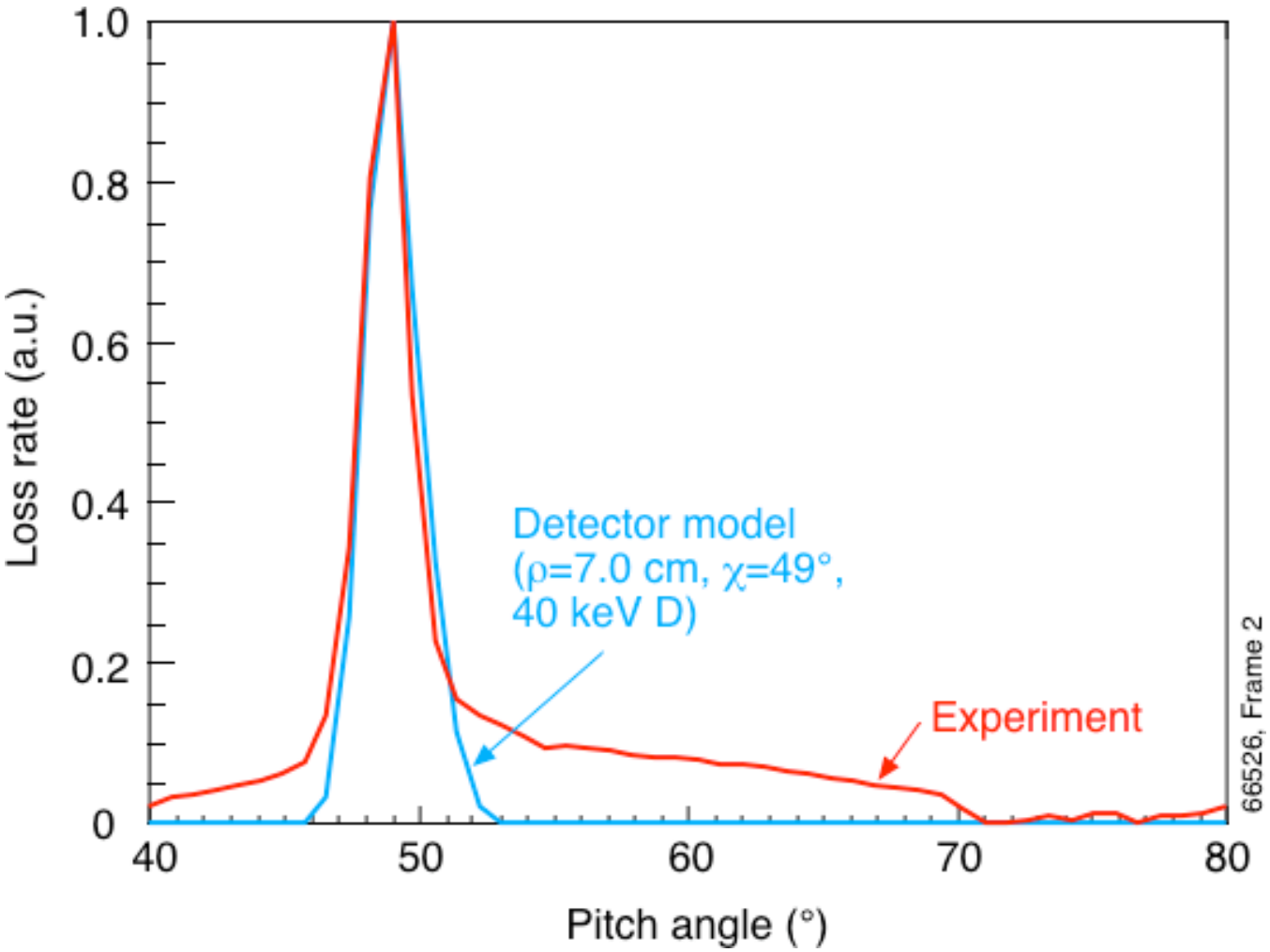

Figure 17: Measured and modeled pitch angle distributions at the detector for the shot shown in Fig. 16. The model curve is computed by detector simulation code and displays the instrumental broadening of a delta function source of particles at 48.5° pitch angle. The measurement and model for that pitch angle are in good agreement, though the measurement also indicates a tail of loss extending to higher pitch angle. This tail is the Category II loss at ρ=7 cm gyroradius. (shot 66526, frame 2.)

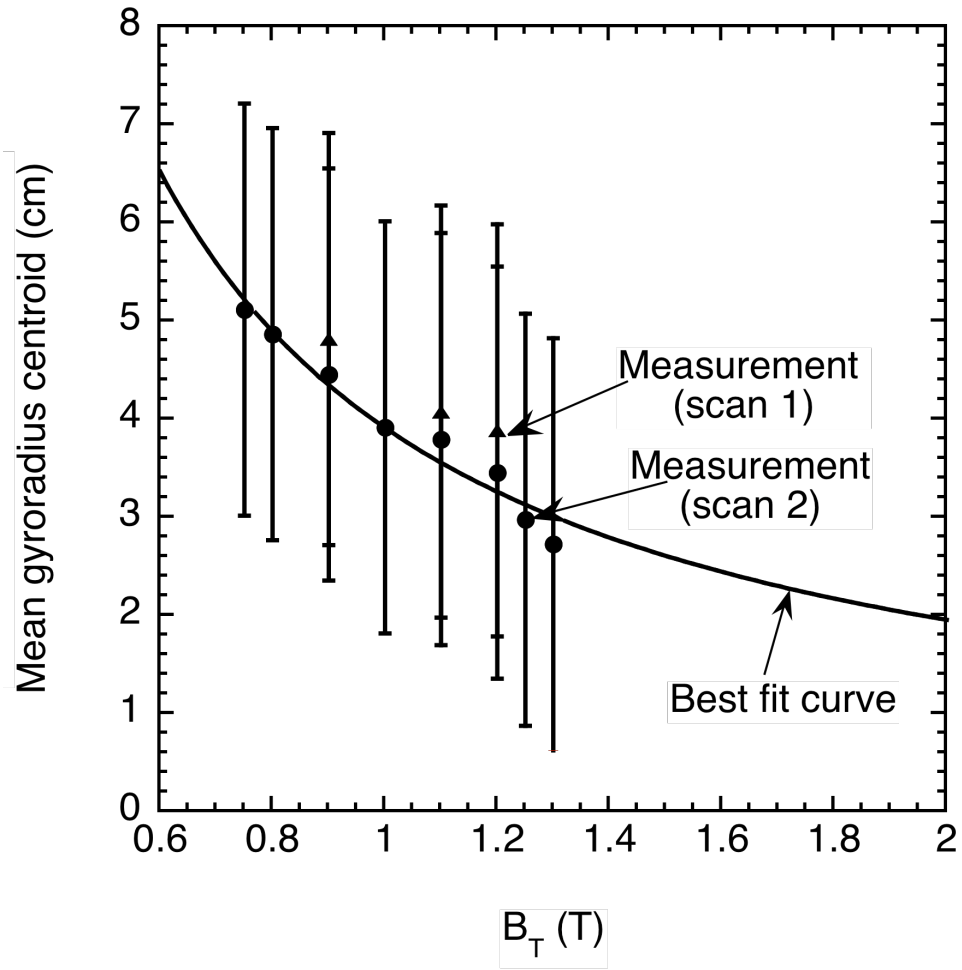

Figure 18: Measured Category I loss gyroradius centroid as B_T is varied. The circles and triangles denote two different experiments during which B_T was scanned, and the results are in good agreement. The solid curve shows the best least squares fit power law function to the data. The best fit is $\rho \propto B^{-1.05}$ with a correlation coefficient of 0.978. The gyroradius is consistent with that expected for 40 keV H ions, indicating that the loss is of the full energy injected ions and is occurring on a time scale short compared to the slowing down time (~12 ms in this condition.)

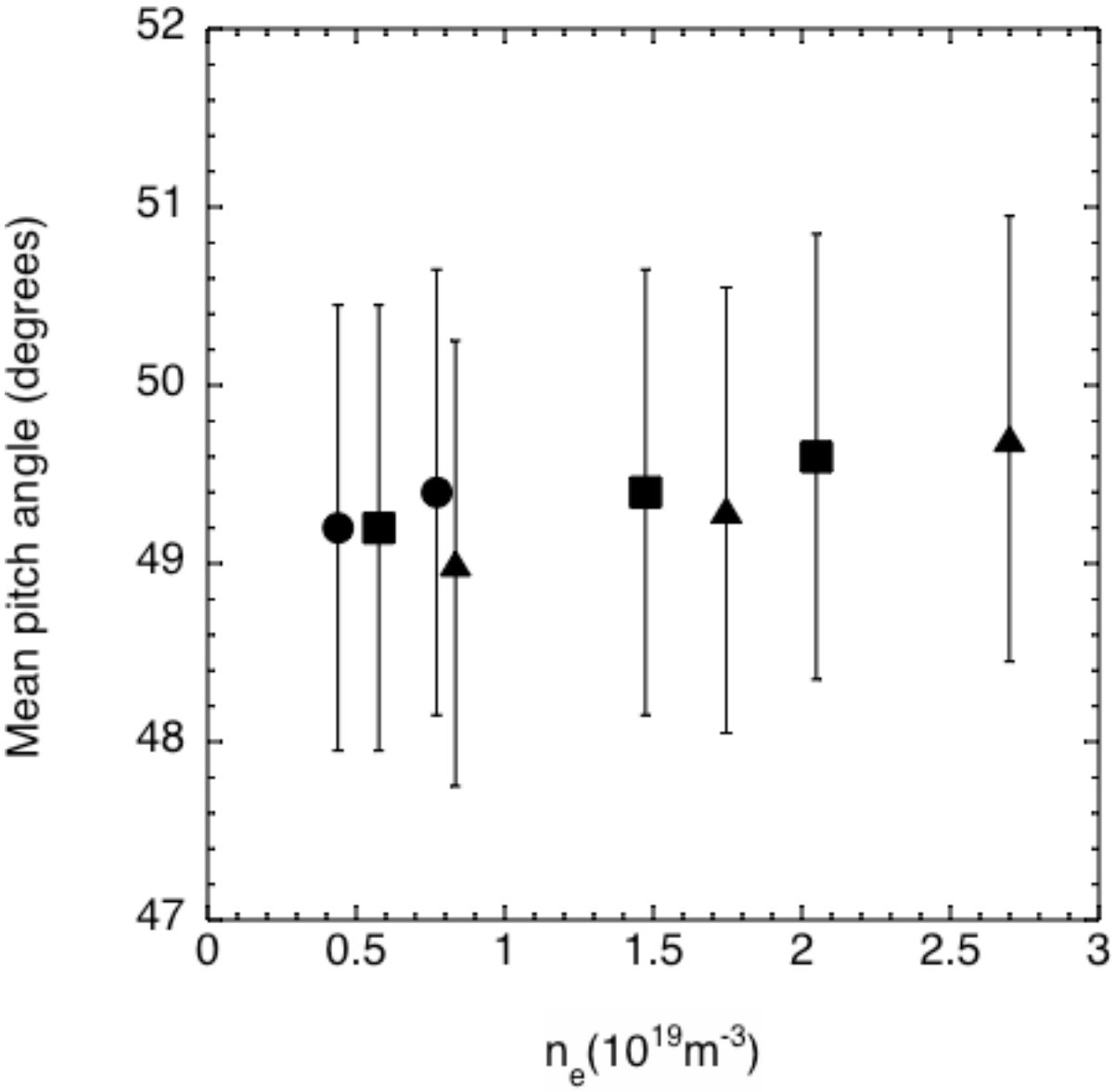

Figure 19: Measured Category I pitch angle as the line average density is varied. Within the errors of measurement, the pitch angle is constant over the entire range of density. This data is taken from three different shots taken at the standard conditions of R_{ax}=94.9 cm, B_T=0.9 T. Circles are from shot 66520, squares are from 66517, and triangles are from 66522.

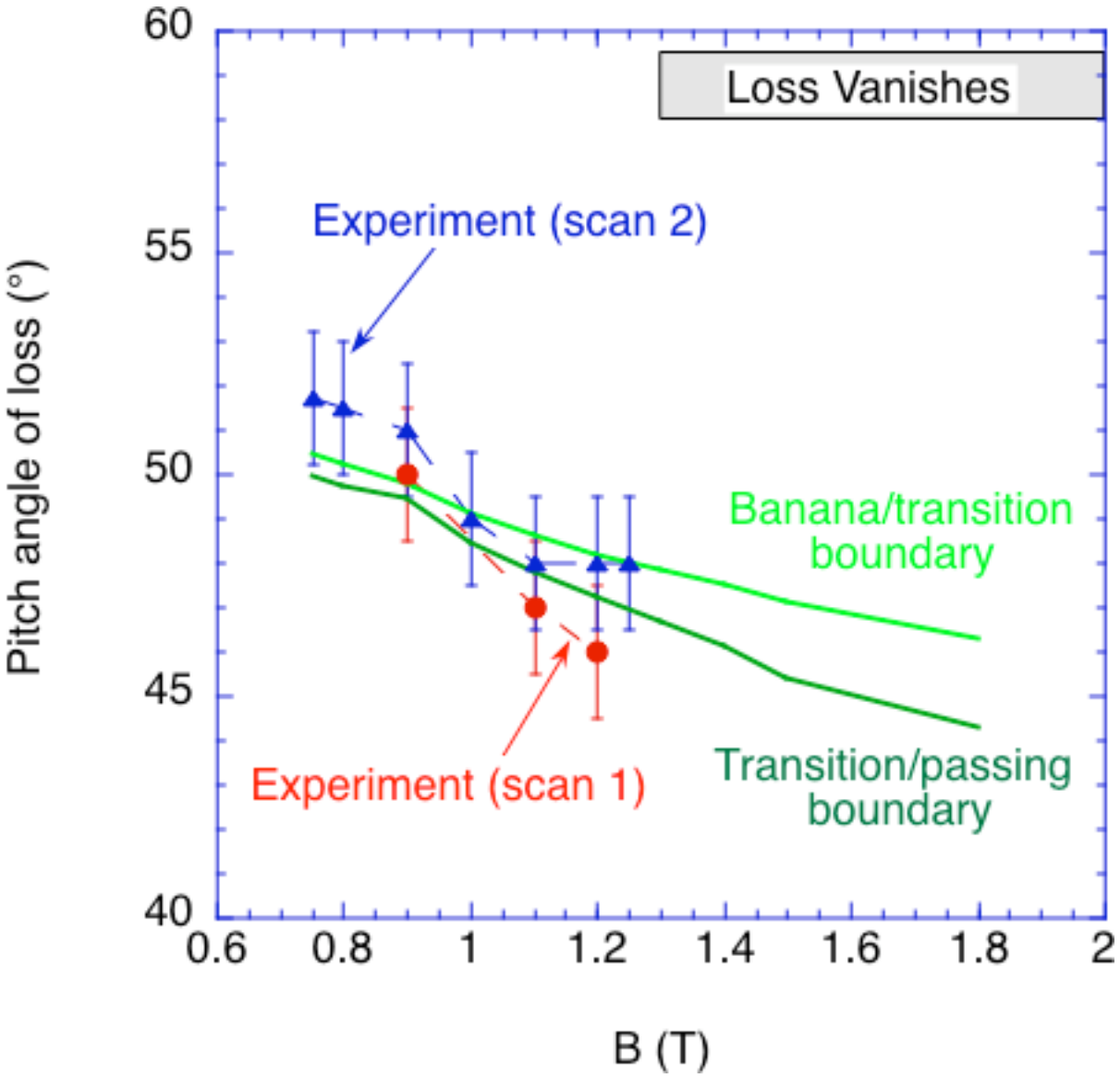

Figure 20: Measured Category I loss pitch angle as B_T is varied. The circles and triangles denote two different experiments during which B_T was scanned, as in Figure 18, and are in agreement within the error bars. Also shown are the pitch angles of the boundaries between trapped and transition orbits and passing and transition orbits. These boundaries have been computed by an orbit code as detailed in the text. As noted in the discussion of Fig. 15, Category I loss is not seen at and above B_T=1.3 T, hence the absence of data points there. Within the error bars, the pitch angle of this Category I loss matches that of the transition orbits computed by the orbit code.

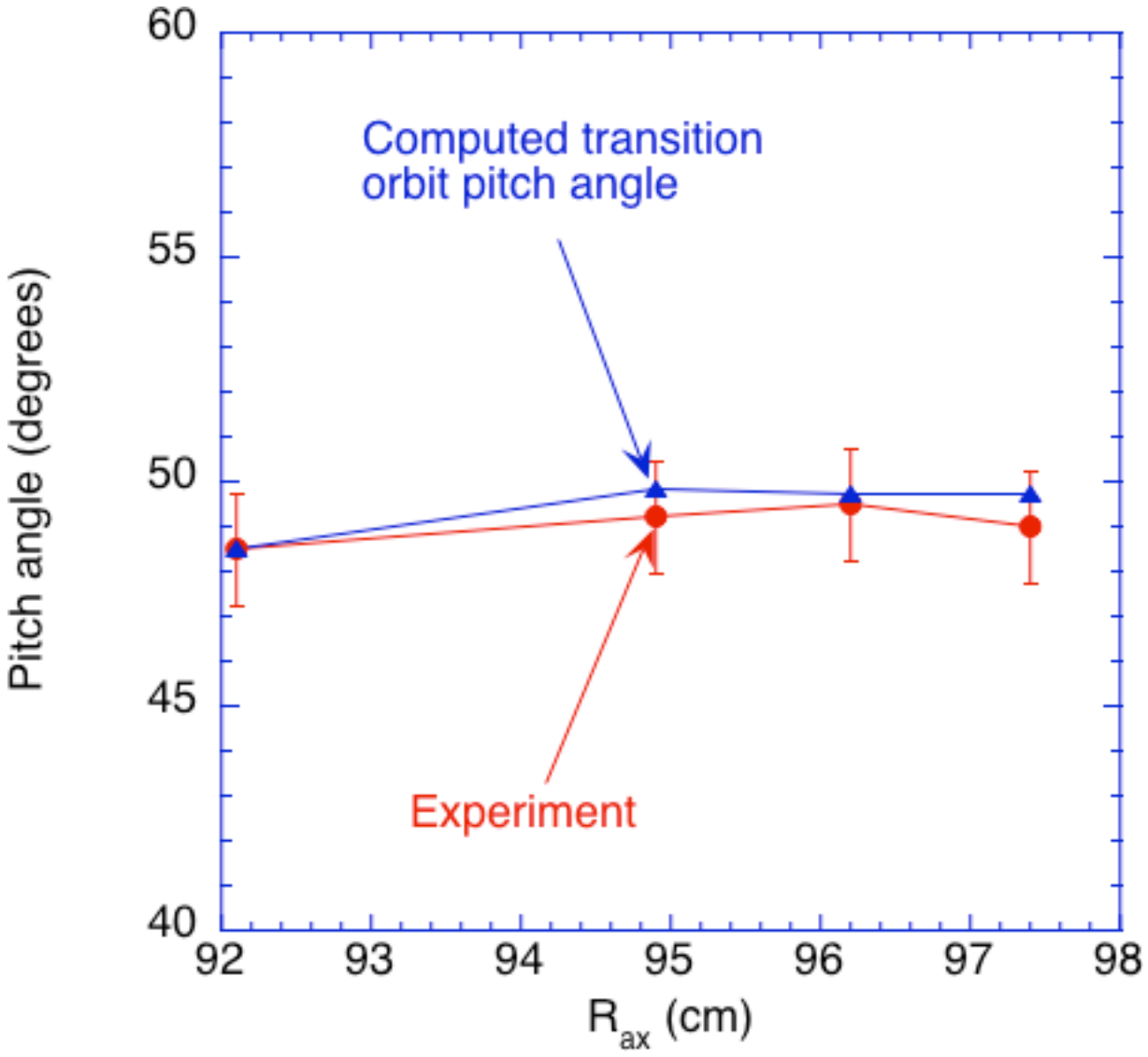

Figure 21: Measured Category I pitch angle as the magnetic axis position, R_{ax}, is varied. Also shown is the transition orbit pitch angle range as determined from orbit calculations with the corresponding magnetic equilibria. Within the errors of measurement, the observed pitch angle of the Category I loss matches that expected of transition orbits.

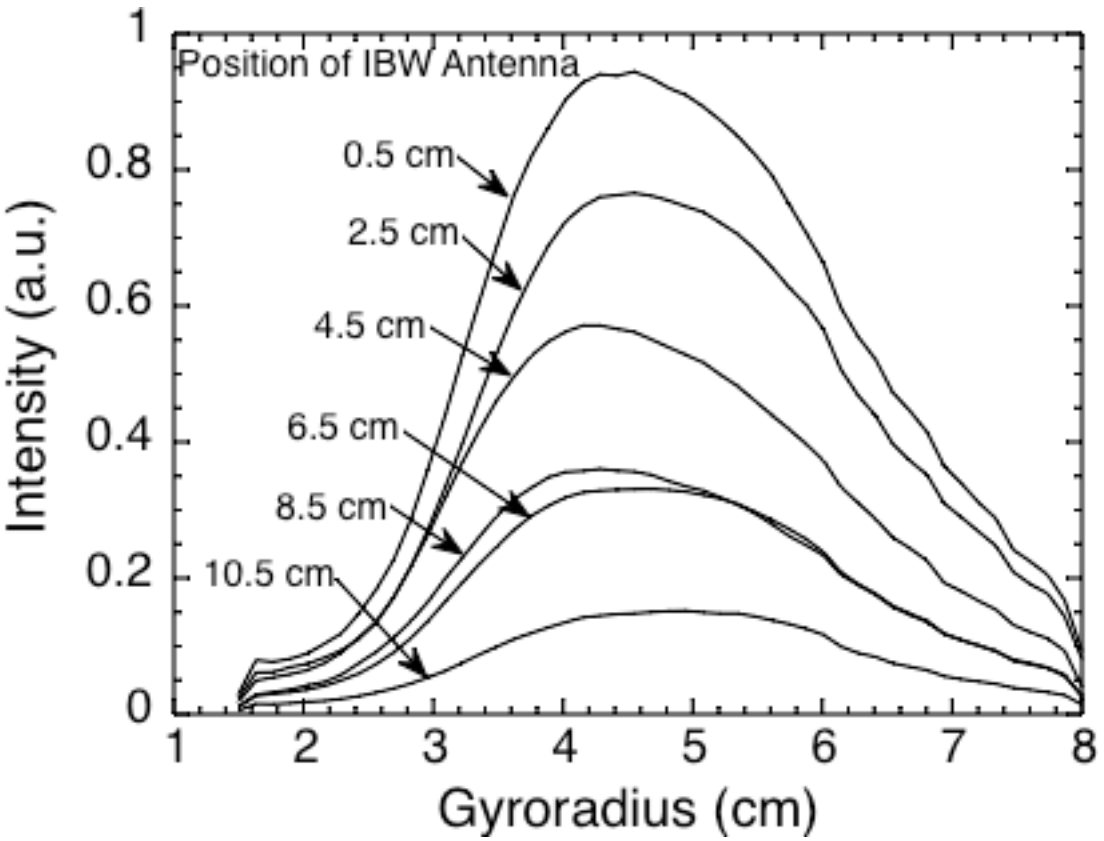

Figure 22: Gyroradius centroid distributions measured during a position scan of the IBW antenna at the outer midplane. The gyroradius centroid distributions are all of similar same shape. This is not surprising since the data described previously are consistent with a monoenergetic loss, i.e. loss at the full injection energy.

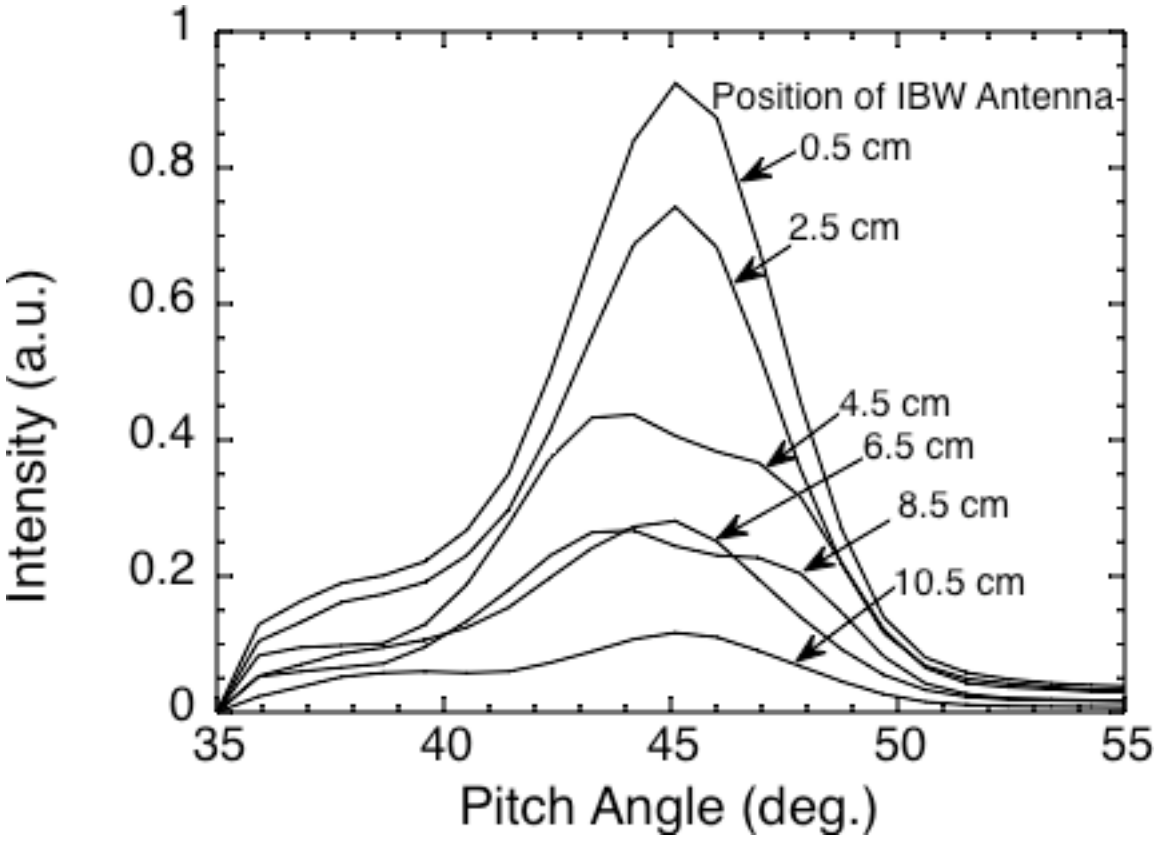

Figure 23: Pitch angle distributions measured during a position scan of the IBW antenna. As the antenna is moved inward, the loss is most strongly diminished for $43° \leq \chi \leq 47°$.

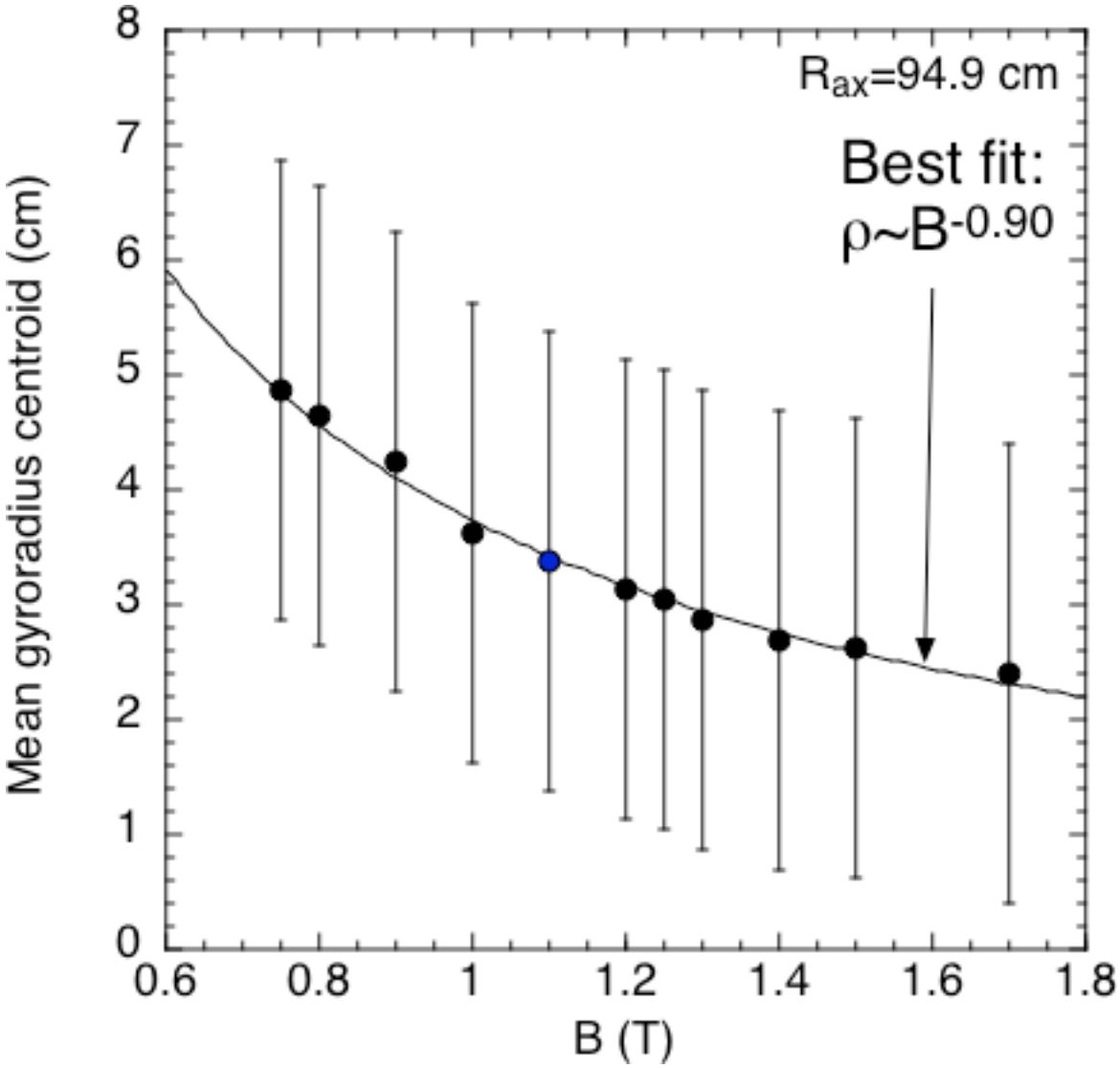

Figure 24: Gyroradius centroid of the Category II (high pitch angle) loss as a function of B_T. The best fit power law form for these points is $\rho \propto B^{-0.903}$, which has a correlation coefficient of 0.993. This is consistent with the loss being at constant energy across the scan, and the gyroradius is consistent with that of the neutral beam's full energy 40 keV H ions.

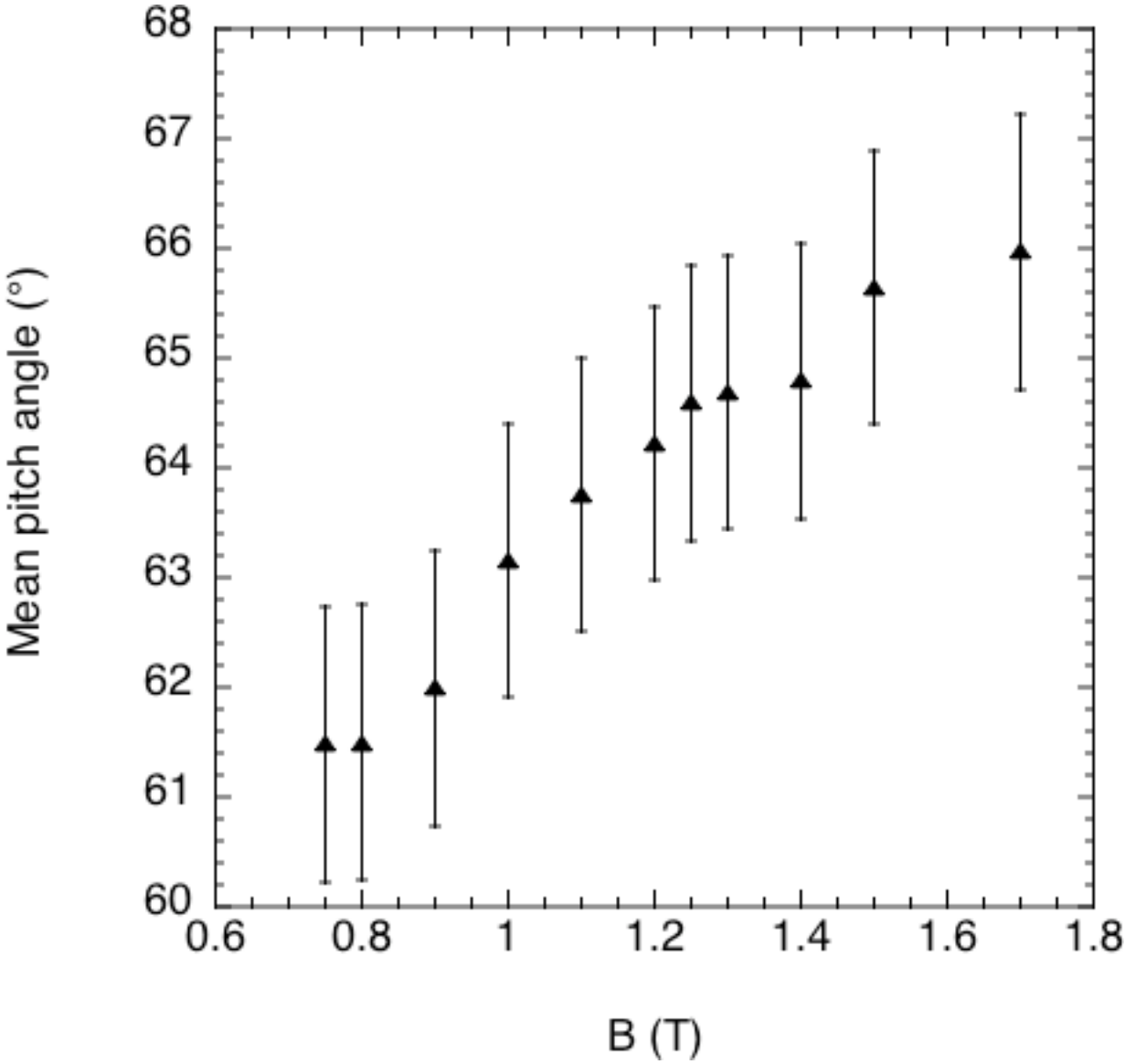

Figure 25: Mean pitch angle of the Category II (high pitch angle) loss as a function of B_T. The reason for this variation is not understood. All data was taken at R_{ax}=94.9 cm.

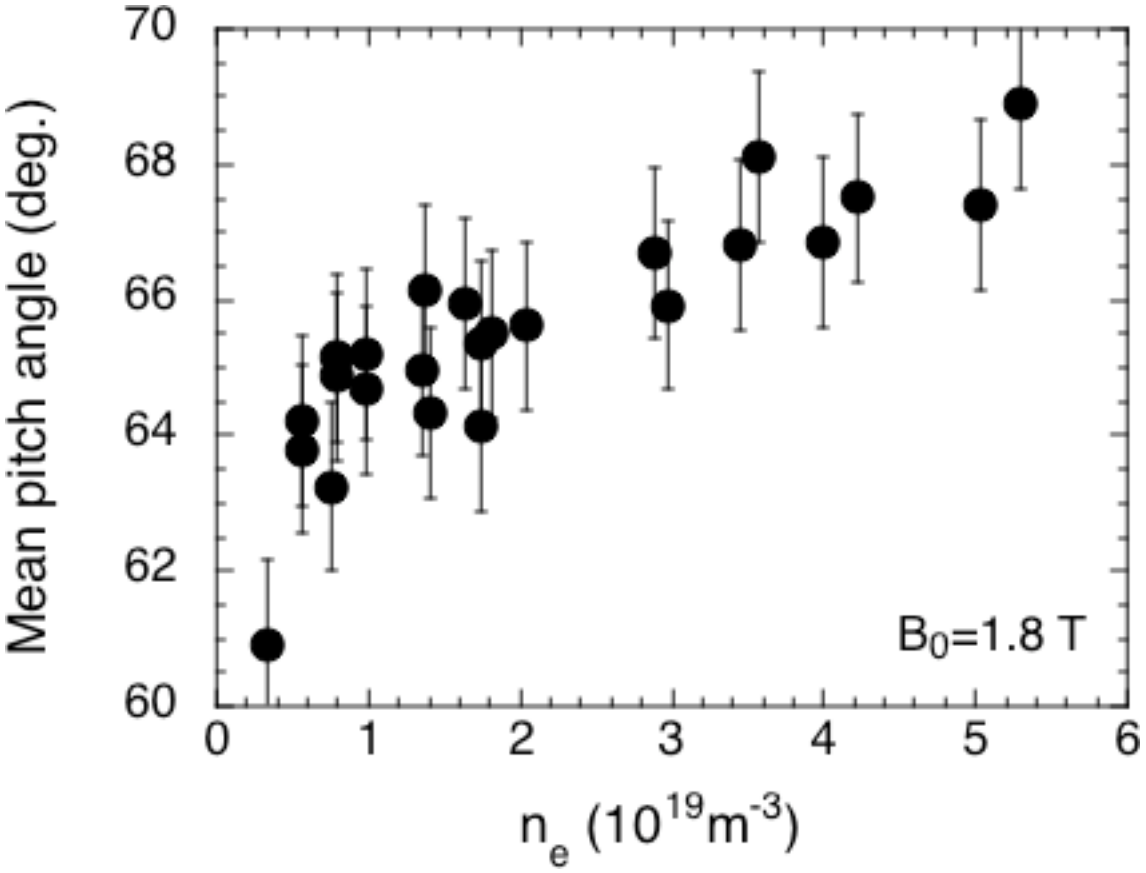

Figure 26: Mean pitch angle of the Category II loss as a function of line average density. The mean pitch angle exhibits a trend of increasing as the density increases. This is counterintuitive as higher pitch angles at the detector arise from particles deposited at smaller minor radius, yet higher density in the discharge should cause the beam ions to be deposited closer to the edge, at larger minor radius.

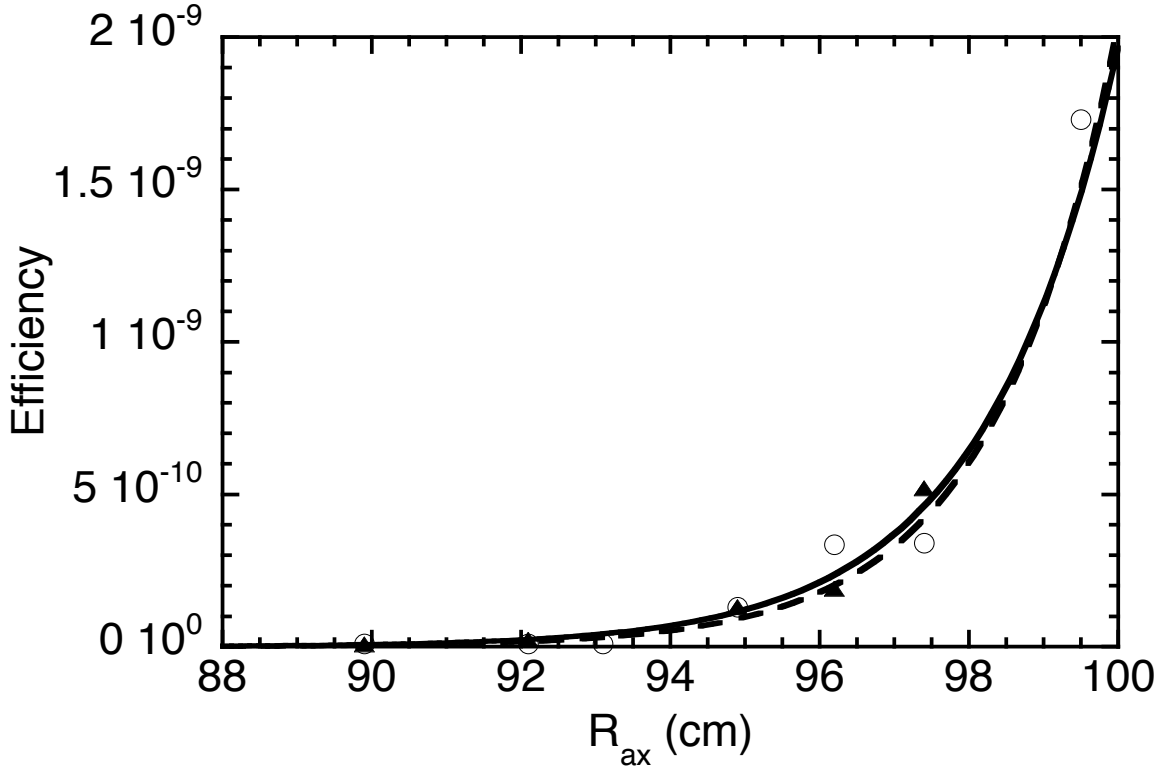

Figure 27: Measured total loss rate (solid triangles) and modeled loss (open circles) as a function of R_{ax}. Exponential curves are fitted to each, and the variation of the model is in good agreement with the observations.

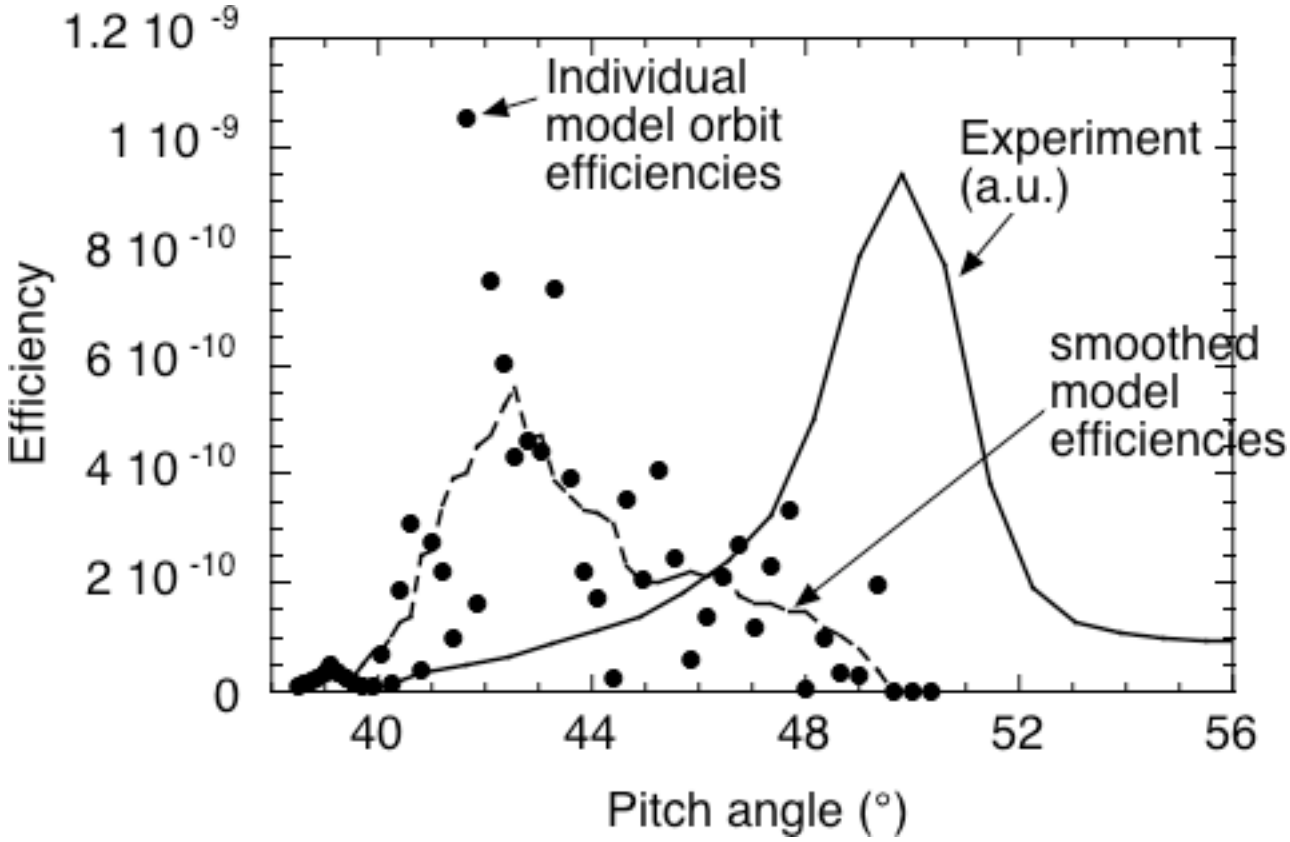

Figure 28: Measured (solid line) and modeled (dashed line and circles) pitch angle distributions for B_T=0.9 T, R_{ax}=94.9 cm. The circles are the detector efficiencies computed for the stated pitch angles using the computational model described in the text. The computational result is clearly very sensitive to the initial conditions. The dashed line is a running average in pitch angle of the discrete points, to allow easier comparison by eye of the measurements and the model. The model does not reproduce the features seen in the measured pitch angle distribution for this condition.

The Princeton Plasma Physics Laboratory is operated
by Princeton University under contract
with the U.S. Department of Energy.

Information Services
Princeton Plasma Physics Laboratory
P.O. Box 451
Princeton, NJ 08543

Phone: 609-243-2245
Fax: 609-243-2751
e-mail: pppl_info@pppl.gov
Internet Address: http://www.pppl.gov